

KEEP CALM AND BARYON: THE DISTRIBUTION OF  
BARYONS AND DARK MATTER ON COSMIC SCALES

BENJAMIN A. COOK

A SENIOR THESIS  
PRESENTED TO THE FACULTY  
OF PRINCETON UNIVERSITY  
IN CANDIDACY FOR THE DEGREE  
OF BACHELOR OF ARTS

RECOMMENDED FOR ACCEPTANCE  
BY THE DEPARTMENT OF  
ASTROPHYSICAL SCIENCES

ADVISOR: PROF. NETA BAHCALL

MAY 2014

I hereby declare that I am the sole author of this thesis.

I authorize Princeton University to lend this thesis to other institutions or individuals for the purpose of scholarly research.

---

Benjamin A. Cook

I further authorize Princeton University to reproduce this thesis by photocopying or by other means, in total or in part, at the request of other institutions or individuals for the purpose of scholarly research.

---

Benjamin A. Cook

# Abstract

We present a compilation of observational measurements of the distribution of baryons, relative to dark matter, in halos ranging in size from galaxies to massive clusters. This includes X-ray and SZ measurements of the hot intracluster medium (ICM) in groups and clusters, weak lensing and optical constraints on the cluster stellar fraction, and absorption measurements of the cool circumgalactic medium (CGM) in galactic halos. Using direct observations when possible, and extrapolations of observed density profiles when necessary, we show that the baryon content within the virial radius matches the cosmic baryon fraction ( $0.164 \pm 0.004$ ) for halos ranging over three orders of magnitude in mass. The baryon distribution is more centrally concentrated in high-mass halos, and more extended in low-mass halos. Using the ratio of stellar fractions in galaxies and clusters, we place a lower limit of 40% on the contributions of individual galaxy halos to the dark matter and baryonic mass of clusters. Averaged on scales larger than the virial radius, the baryonic mass is a strong tracer of the underlying dark matter distribution, and can be useful as a tool in cosmological studies of structure formation.

# Acknowledgements

First and foremost, I would like to thank Neta Bahcall for her wonderful support and guidance throughout this project, my graduate application process, and my entire Princeton career. She is an inspiration and invaluable mentor to every student in astrophysics and made me feel welcome in the department from my first day on campus. I'm very glad to have gotten the chance to conclude my senior year by working with her on this project, and I look forward to collaborating more on it in the future. I would like to thank Professor J. Xavier Prochaska, Professor Lars Hernquist, and Dr. Shy Genel for their discussions and insight into their work. I would also like to thank Dr. Renyue Cen for making his simulations available for my analysis, which I regret I was not able to include in this thesis. Thank you to Tomer, Michael, Fred, and all the astro undergrads for the great times studying and working together in Peyton. Thank you to Shelby for believing in me, for giving me a reason to try harder and reach my full potential, and for always lifting my spirits when work is overwhelming. Finally, I would like to thank my parents, Kelly and Tom, for their love and encouragement and for giving me the opportunity to make it where I am today.

Dedicated to my brother, Walter.

I'm very proud of you, and know you will accomplish amazing things.  
Continue to challenge yourself, and I'll enjoy my headstart while it lasts.

# Contents

Abstract . . . . .	iii
Acknowledgments . . . . .	iv
<b>1 Introduction</b>	<b>1</b>
1.1 The Cosmic Matter-Energy Components . . . . .	1
1.2 The Cosmic Baryon Fraction . . . . .	2
1.3 The Cluster Missing Baryon Problem . . . . .	9
1.4 The Galaxy-Halo Missing Baryon Problem . . . . .	14
1.5 Our Investigation – Where are the Baryons? . . . . .	16
<b>2 Observations and Data Analysis</b>	<b>18</b>
2.1 Total Mass in Groups and Clusters . . . . .	18
2.2 Cluster Gas Mass Fraction . . . . .	20
2.2.1 Observations . . . . .	21
2.2.2 Extrapolation of Gas Density Profiles . . . . .	26
2.3 Cluster Stellar Mass Fraction . . . . .	30
2.4 Galaxy Mass Fractions . . . . .	32
2.4.1 The Circumgalactic Medium . . . . .	32
2.4.2 Estimate of The Galactic Halo Baryon Fraction . . . . .	34
<b>3 Results</b>	<b>37</b>
3.1 The Distribution of Gas and Baryons in Groups and Clusters . . . . .	37

3.2	The Baryonic Content of Dark Matter Halos . . . . .	43
<b>4</b>	<b>Discussion</b>	<b>46</b>
4.1	Limitations and Observational Biases . . . . .	46
4.1.1	Assumption of Hydrostatic Equilibrium in Calculating Total Mass	46
4.1.2	Gas Clumping in Cluster Outskirts . . . . .	48
4.1.3	Extrapolation of the Density Profile Slope . . . . .	50
4.2	Comparison to Simulations . . . . .	51
4.3	Implications . . . . .	54
4.3.1	Deviations from Self-Similarity . . . . .	55
4.3.2	The Contribution of Individual Galaxies to Clusters . . . . .	56
4.3.3	Where are the Baryons? . . . . .	59
<b>5</b>	<b>Summary and Conclusions</b>	<b>61</b>
	<b>Bibliography</b>	<b>69</b>

# Chapter 1

## Introduction

### 1.1 The Cosmic Matter-Energy Components

After the big bang, the energy content of the universe was distributed in a diverse number of components. As the universe expanded and cooled, the available energy settled down into the primary energy components we observe today, including radiation (photons and neutrinos), baryons (“ordinary” matter, comprised of protons, neutrons, and electrons), as well as the mysterious dark matter and dark energy.

Energy did not populate these forms in equal proportions; the energy densities of each component differed by many orders of magnitude, initially, and their ratios changed continually throughout the expansion history of the universe. Radiation density – primarily the photon density ( $\rho_\gamma$ ), dominant in the earliest periods after the big bang – diluted quickly from the combination of expansionary volume increase and Doppler redshifting. The matter density –  $\rho_m$ , comprised of both baryons ( $\rho_b$ ) and cold dark matter ( $\rho_c$ ) – was initially only a minuscule portion of the cosmic energy budget, but eventually matter dominated the cosmic scene after expansion “cooled” the photon temperature significantly. Initially insignificant relative to the energy content of the other components, dark energy –  $\rho_\Lambda$ , commonly thought to



be a cosmological constant  $\Lambda$  – retains a constant energy density while the universe expands and became dominant at late times when  $\rho_m$  had decreased significantly. Each of these energy densities are often scaled by the critical density required to stop cosmic expansion:

$$\rho_{crit} = \frac{3H^2}{8\pi G} \quad (1.1)$$

with  $H$  the Hubble parameter and  $G$  Newton’s constant. The density of each component relative to the critical density is expressed as  $\Omega$ . For example:

$$\frac{\rho_b}{\rho_{crit}} = \Omega_b . \quad (1.2)$$

## 1.2 The Cosmic Baryon Fraction

Baryons and dark matter, the two components of the total matter density, have the same dependence on the expansionary scale factor and redshift. Since the total matter density is just their sum, the total matter density also scales identically:

$$\begin{aligned} \rho_c \propto \rho_b \propto \rho_m \propto a^{-3} \\ \propto (1+z)^3 . \end{aligned} \quad (1.3)$$

Therefore, we see that the ratio of baryons to dark matter will remain constant at its primordial level throughout the history of the universe. A useful and commonly studied constant is the *cosmic baryon fraction*,  $f_b$ , the fraction of all matter in baryonic form:

$$f_b = \frac{\rho_b}{\rho_b + \rho_c} = \frac{\rho_b}{\rho_m} = \frac{\Omega_b}{\Omega_m} . \quad (1.4)$$

The above argument, that the baryon fraction remains constant throughout cosmic history, applies only in the homogeneous regime, when there are no spatial variations in the overall mass density. If inhomogeneities exist, self-interactions lead to the com-

plicated evolution of structure. While dark matter (by energy density) dominates the gravitational collapse of inhomogeneities and drive the growth of structure, it is obvious that the baryonic abundance plays an incredibly important role in determining the makeup of our universe. Dark matter interacts only through gravity, but baryons are subject to electromagnetic forces, thermal emission, collisions, and numerous other interactions collectively known as “baryonic physics”. Baryons are solely responsible for all non-gravitational phenomena studied in physics and astrophysics: the formation of galaxies, stars, and planets, supernovae, radiation, magnetism, chemistry, and, eventually, life itself.

These baryonic effects lead to a divergence between the baryonic and dark matter distributions, and hence a variation in the local baryon fraction. Although the local baryon fraction may vary hugely from place to place, it is possible to estimate the cosmic baryon fraction by averaging over a substantially large volume. By studying the baryon fraction (and what forms the baryons take) we can learn about the relative distributions of dark matter and baryons, and the contributions of baryonic and gravitational physics to the formation of structure.

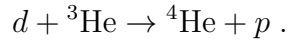
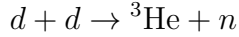
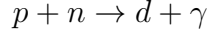
The baryon and dark matter abundances were major factors in several important physical processes in the early universe. Through observable signatures of these processes, cosmologists have been able to place powerful constraints on the cosmic baryon fraction at these early times. Consistent with the literature, we will consider the baryon fraction inferred from these methods to be the cosmic fraction against which we will compare measurements from the local, highly inhomogeneous universe.

One mechanism that constrains the baryonic abundance is big bang nucleosynthesis (BBN), the process which generated the first light elements beyond hydrogen<sup>1</sup>. In the first seconds after the big bang, the only ordinary matter particles which existed (and were stable) were protons ( $p$ ), electrons ( $e$ ), neutrons ( $n$ ), and deuterium ( $d$ ).

---

<sup>1</sup>The discussion which follows is guided primarily by Chapter 3.2 of Weinberg (2008), a useful but relatively technical reference on the topic.

The high temperatures and densities of nucleons allowed the conversion of protons and neutrons into more complex and heavier nuclei, through processes such as:



The BBN reactions began around 100 – 200 seconds after the big bang (Weinberg, 2008). The exact time when these reactions reached thermal equilibrium depends weakly on the abundance of baryons,  $\Omega_b h^2$ , where  $H_0 = 100h \text{ km s}^{-1} \text{ Mpc}^{-1}$  defines  $h$ , an important scaling factor<sup>2</sup>. After the universe expanded and cooled sufficiently, these reactions fell out of equilibrium, leaving the universe enriched with helium ( ${}^4\text{He}$  and  ${}^3\text{He}$ ) and trace amounts of elements such as deuterium and lithium ( ${}^7\text{Li}$ ). The higher  $\Omega_b h^2$ , the more complete the transformation of  $n$  and  $d$  into helium. Therefore, the baryon abundance strongly affects the resulting abundance of deuterium and residual elements like lithium and  ${}^3\text{He}$ . Figure 1.1 shows the dependence of these primordial abundances on the cosmic baryon abundance.

The baryon abundance can be determined through observational constraints of, for example, the deuterium abundance, which among the byproducts of BBN depends most strongly on  $\Omega_b h^2$ . The deuterium abundance has been inferred from variety of sources, including from the Milky Way’s ISM (Linsky et al., 1993, 1995), absorption towards QSOs (Tytler et al., 1996; Kirkman et al., 2003), and even from measurements of the composition of the Jovian atmosphere (Niemann et al., 1996). All such methods have limitations, as deuterium can be destroyed in stellar (and brown dwarf) cores, altering the deuterium abundance slightly with time. Iocco et al. (2009) provides

---

<sup>2</sup>Uncertainties on the true expansion rate ( $h$ ) translate into uncertainties on a number of observables such as matter abundances ( $\Omega$ ) and halo properties (M or r). Therefore, many derived properties in the literature are often given in terms of  $h_{70} \equiv H_0/70 \text{ km s}^{-1} \text{ Mpc}^{-1}$ .

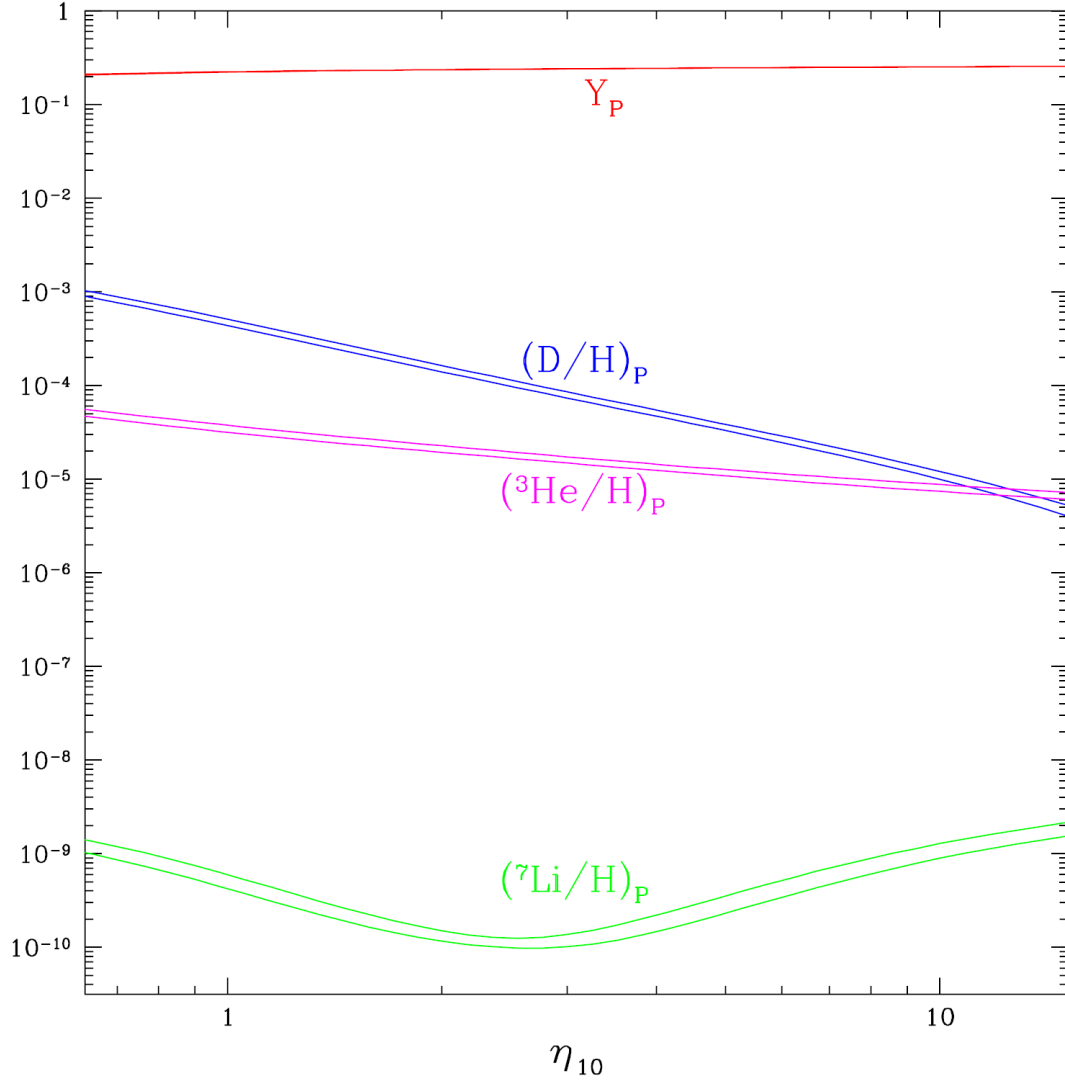


Figure 1.1: The BBN-predicted primordial abundances of deuterium (D),  ${}^3\text{He}$ ,  ${}^7\text{Li}$ , and  ${}^4\text{He}$  ( $Y_P$ ), as a function of the baryon abundance parameter  $\eta_{10} \approx 274 \times \Omega_b h^2$ . The width of the curves represents the uncertainties in various nuclear reaction rates. Figure taken from Steigman (2006, Fig. 1), another helpful overview of BBN physics.

a compilation of deuterium abundance measurements, placing a constraint on the baryon abundance of  $\Omega_b h^2 = 0.021 \pm 0.001$ . Observed  ${}^7\text{Li}$  abundances are a factor of a few lower than predicted from BBN, suggesting that there could be additional physics responsible for destroying lithium (Suzuki et al., 2000; Meléndez & Ramírez, 2004). This is known as the “Lithium Problem,” and is still an unsolved problem in interpreting BBN.

A complementary method of inferring the baryon abundance at early times is from measurements of the acoustic peaks in the Cosmic Microwave Background (CMB) power spectrum. The CMB power spectrum contains large peaks, representing correlations in the CMB on particular scales. In the first few hundred thousand years after the big bang, the temperature of the universe was high enough to keep atoms fully ionized into separate nuclei and electrons. These charged particles were strongly coupled to the local photon field through electromagnetic interactions, so that the two components combined to form what is called a photon-baryon fluid. This fluid fell towards the centers of gravitational wells created by dark matter. However, unlike the non-interacting dark matter, the photon-baryon fluid’s pressure rose when its density rose, stopping its infall. The pressure build-up forced the fluid back out of the well until its pressure dropped enough to allow gravity to draw it back once again. These ongoing fluctuations in the pressure and density of the fluid were frozen into the CMB power spectrum as the acoustic peaks. This occurred when the average temperature of the universe dropped sufficiently to allow neutral atoms to form, and the CMB photons began streaming freely through the universe<sup>3</sup>.

The baryon abundance at this early time had several effects on the acoustic peaks in the CMB, as did the overall mass abundance ( $\Omega_m h^2$ ). Figure 1.2 shows how changes in these abundances are reflected in the acoustic peaks. The location of the first peak (and all subsequent peaks) is determined by the sound speed at the epoch of last scat-

---

<sup>3</sup>For an introductory discussion on the concept of acoustic peaks in the CMB, see Chapter 9 of Ryden (2003).

tering. This sound speed increases when  $\Omega_b h^2$  increases, although it is more sensitive to changes in  $\Omega_m h^2$ , an increase of which results in a decrease in the sound speed (Mukhanov, 2005, ch. 9.8). The relative heights of the acoustic peaks is a further diagnostic of the baryon abundance. As seen in Figure 1.2, odd-numbered peaks are higher than even-numbered peaks in a universe with high  $\Omega_b h^2$ . This is because an increase in the amount of massive baryons reduces the frequency of acoustic oscillations (Dodelson, 2003, ch. 8.7.3). Finally, the power spectrum declines towards higher multipoles ( $l$ ) due to a process known as “Silk Damping”. This damping term is due to imperfections in the photon-baryon coupling, and the characteristic damping scale is influenced by  $\Omega_b h^2$  (Durrer, 2008, ch. 4.7).

Through a combination of all the processes listed above, modern CMB observations have been able to place strong constraints on both  $\Omega_b h^2$  and  $\Omega_m h^2$ . Two of the most noteworthy such measurements come from the *Wilkinson Microwave Anisotropy Probe* (*WMAP*, Bennett et al., 2003) and the *Planck* Satellite (Planck Collaboration, 2013a). Different constraints are placed on these parameters depending on what additional data<sup>4</sup> is included in the analysis. We will take the median value (from each paper) of parameters derived through these various methods, and we use the systematic variance in the parameters as the uncertainty, if it is larger than the statistical uncertainty listed from the analysis.

From the 9-year data release of *WMAP* (*WMAP9*, Hinshaw et al., 2013), we take values  $\Omega_b h^2 = 0.02229 \pm 0.00035$  and  $\Omega_c h^2 = 0.1138 \pm 0.0032$ . From the results paper of *Planck* (Planck Collaboration, 2013b), we take the values  $\Omega_b h^2 = 0.022115 \pm 0.00025$  and  $\Omega_c h^2 = 0.11957 \pm 0.0025$ . These values allow us to constrain the cosmic baryon

---

<sup>4</sup> $H_0$ , BAO, polarization, etc.

fraction as:

$$\begin{aligned}
f_b &= \frac{\Omega_b h^2}{\Omega_b h^2 + \Omega_c h^2} \\
&= 0.164 \pm 0.004 \text{ (} WMAP9 \text{)} \\
&= 0.156 \pm 0.003 \text{ (} Planck \text{)}
\end{aligned}
\tag{1.5}$$

The uncertainty on  $f_b$  comes from the propagation of uncertainties on  $\Omega_b h^2$  and  $\Omega_c h^2$ :

$$\begin{aligned}
\Delta f_b &= \sqrt{\left(\frac{\partial f_b}{\partial \Omega_b h^2}\right)^2 \Delta(\Omega_b h^2)^2 + \left(\frac{\partial f_b}{\partial \Omega_c h^2}\right)^2 \Delta(\Omega_c h^2)^2} \\
&= \sqrt{\left(\frac{\Omega_c h^2 \Delta(\Omega_b h^2)}{(\Omega_b h^2 + \Omega_c h^2)^2}\right)^2 + \left(\frac{\Omega_b h^2 \Delta(\Omega_c h^2)}{(\Omega_b h^2 + \Omega_c h^2)^2}\right)^2} \\
&= \frac{1}{(\Omega_m h^2)^2} \sqrt{[\Omega_c h^2 \Delta(\Omega_b h^2)]^2 + [\Omega_b h^2 \Delta(\Omega_c h^2)]^2}
\end{aligned}
\tag{1.6}$$

It is commonly discussed (e.g., Spergel et al., 2013) that the *Planck* results yield  $\Omega_m$  significantly higher and  $H_0$  significantly lower than other previous measurements, including *WMAP*. This results in the lower value of  $f_b$  as derived from *Planck*. Earlier estimates (e.g., *WMAP5*, Dunkley et al., 2009) placed  $f_b$  around 0.17, a canonical value which is often used in the literature. Because of the issues surrounding the interpretation of the Planck data, we will use the WMAP9 measurement of  $f_b \approx 0.164$  for our primary comparisons with low-redshift baryon fractions, although we will attempt to also compare to the Planck constraints whenever possible. One limitation of this work is the relative uncertainty on the “cosmic” baryon fraction due to the discrepancies in CMB observations. We hope that subsequent analysis of the *WMAP/Planck* disagreements will solve this problem, one way or another.

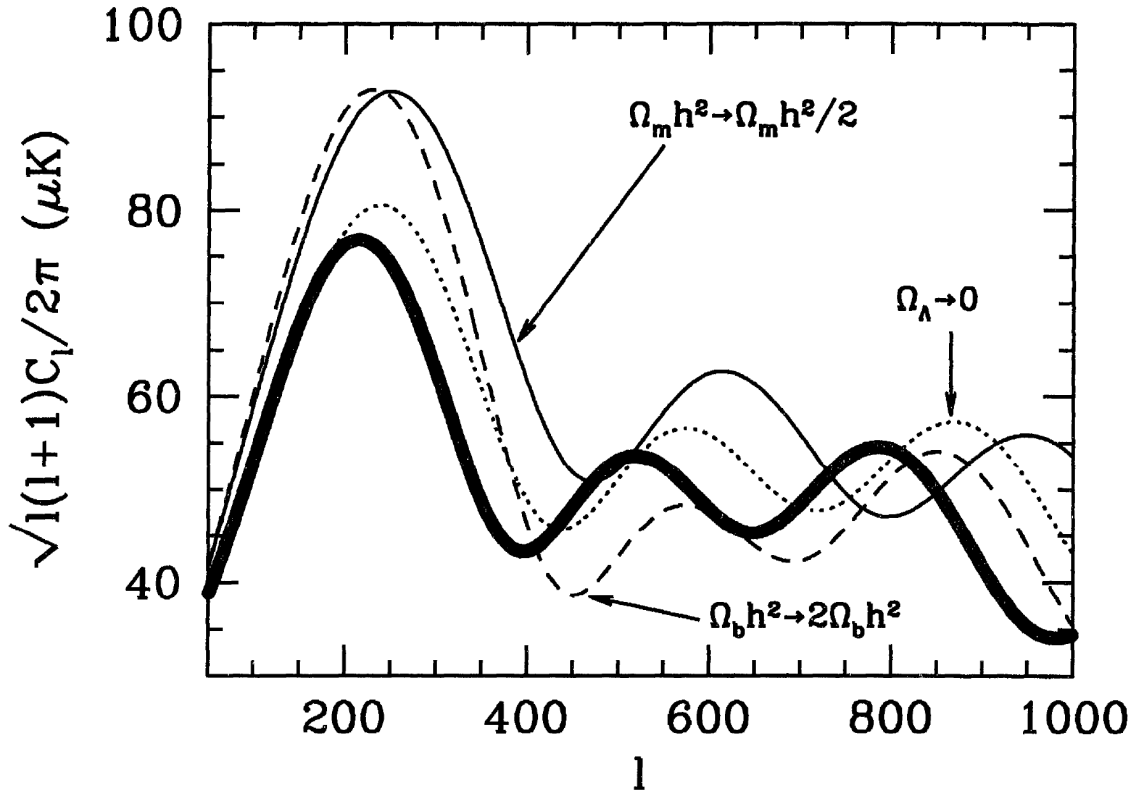


Figure 1.2: The variation in the CMB power spectrum's acoustic peaks due to variations in cosmic abundance parameters. The thick black line represents a fiducial universe with  $\Omega_m h^2 = 0.16$ ,  $\Omega_b h^2 = 0.021$ , and  $\Omega_\Lambda = 0.7$ . Other lines represent the results from changes to these parameters, notably an increase in peak height and rightward shift of peaks ( $\Delta l > 0$ ) with an increase in  $\Omega_b h^2$ . A decrease in  $\Omega_m h^2$  has similar (but distinguishable) effects. Figure from Dodelson (2003, Fig. 8.19).

### 1.3 The Cluster Missing Baryon Problem

Large *galaxy clusters* represent the most massive dark matter halos which have had adequate time to virialize since the big bang. The richest clusters often contain hundreds of large galaxies, while much smaller *groups* may contain several to tens of galaxies. The galaxies are bound to the gravitational well of the combined mass of the cluster, which includes dark matter as well as baryons. Some clusters show a steep pressure profile (and a flat density profile) towards their centers, suggesting that they are dynamically *relaxed* and possess a *cool core* (these are known as CC clusters).



Clusters with flattened central pressure profiles (and cuspy density profiles) are *unrelaxed* or *non-cool core* (NCC) clusters. Because they are the largest bound objects in the universe, clusters offer one of the best ways of measuring the baryon fraction at low-redshift: they have collapsed from large volumes and therefore represent the largest samples of the cosmic dark matter and baryon densities that are not in dramatic dynamical evolution. Additionally, their extremely deep gravitational potential wells are expected to prevent any significant fraction of baryons from escaping the system through feedback effects, such as winds, supernovae, or AGN activity.

The baryonic component of galaxy clusters is not primarily stored in galaxies, but in a hot ( $kT \gtrsim 1$  keV), diffuse gas known as the *Intracluster Medium* (ICM). The ICM can be detected through the X-ray brehmsstrahlung emission of the ionized plasma. X-ray telescopes such as *Chandra*, *ROSAT*, *Suzaku*, and *XMM-Newton* have been key in detecting the ICM and constraining its distribution and total mass (e.g., Vikhlinin et al., 2006; Eckert et al., 2012). A complementary method of detecting and measuring the intracluster gas is through the thermal Sunyaev-Zeldovich effect (SZ, Sunyaev & Zeldovich, 1972), which occurs when the energy spectrum of background CMB photons passing through the cluster is altered, due to inverse-Compton scattering with the charged particles in the plasma.

The stars of individual galaxies make up the remainder of the baryonic mass in clusters. Stellar mass is often derived from the luminosity in starlight, which is converted into mass using typical stellar mass to light ratios derived for individual galaxies (Bahcall & Kulier, 2014).

The total mass of clusters is derived through stacked weak-lensing analysis, where the average distortion of background galaxies is measured as a function of cluster-centric radius. These distortions can be inverted to compute the distribution of mass in the cluster which is responsible for the gravitational lensing distortions. Recent weak-lensing analyses (Mandelbaum et al., 2008; Sheldon et al., 2009a) yield accurate

constraints on the total mass of clusters, and show that the distribution of mass is fit well by the Navarro-Frenk-White profile (NFW, Navarro et al., 1996), a prediction from N-body simulations of cold dark matter.

Before addressing the overall masses and sizes of galaxy clusters, it is crucial to outline the definitions for these scales we will use throughout this paper. Because dark matter halos are believed to be self-similar (scaling only by overall mass or central density) their sizes are often given relative to fixed overdensities  $\Delta$ , the location where the density of matter interior is a particular multiple of the critical density of the universe. For example,  $\Delta = 200$  equates to the region in a halo where

$$\rho_m(< r) = \frac{3M(< r)}{4\pi r^3} = 200 \times \rho_{crit} . \quad (1.7)$$

The mass and radius of a galaxy cluster is typically measured at a characteristic overdensity. For example, many sources in the literature list the cluster mass and radius as  $M_{500}$  and  $r_{500}$ , measured at an overdensity of  $\Delta = 500$ . As cluster mass is clustered towards the center,  $\Delta$  decreases towards larger cluster-centric radii. The gravitational system virializes around  $\Delta = 100$  (Eke et al., 1996), so we take the characteristic scales of clusters to be the virial (or halo) mass and radius,  $M_{vir} \equiv M_{100}$  and  $r_{vir} \equiv r_{100}$ .

Through stacked weak lensing measurements, rich galaxy clusters have been observed to have halo masses of  $10^{14} - 10^{15} M_{\odot}$  (Mandelbaum et al., 2008), and halo radii of around  $1 - 3$  Mpc (Vikhlinin et al., 2006). Lower-mass “groups” typically have masses around  $10^{13} - 10^{14} M_{\odot}$ , and represent the intermediate range between the most massive clusters and large galaxies. The self-similarity of group and cluster halos results in a fairly constant relation between masses or radii at various overdensities. For example (Rasheed et al., 2011):

$$r_{vir} \approx 1.3 \times r_{200} \approx 1.9 \times r_{500} . \quad (1.8)$$

Using an approximate mass density profile of  $\rho_m \propto r^{-2.5}$  in these outer cluster regions, we assume that the total mass scales roughly as  $M \propto r^{0.5}$ , so that

$$M_{vir} \approx 1.14 \times M_{200} \approx 1.38 \times M_{500}. \quad (1.9)$$

Recent X-ray and SZ measurements have begun to illuminate the hot intracluster plasma, allowing detailed study of these large reservoirs of baryons in groups and clusters. X-ray surface brightness observations, in particular, are able to directly measure the gas density profile and therefore retrieve the mass. However, because brehmsstrahlung emission declines with the square of the gas density, accurate X-ray measurements have typically been limited to the inner regions of halos. Early studies of this kind in clusters include Vikhlinin et al. (2006, with *Chandra*) and Arnaud et al. (2007, with *XMM-Newton*), while Sun et al. (2009) made similar measurements of the hot gas in groups using *Chandra*. Measuring the gas mass fraction only out to  $r_{500}$ , these observations typically found  $f_{gas}(< r_{500}) \lesssim 10\text{--}12\%$ , well below the cosmic baryon fraction, although with large variance between clusters. Importantly, there is a clear trend towards lower gas content in lower-mass halos: nearly all groups and small clusters show gas fractions well below 10% at  $r_{500}$ . The stellar fraction in clusters has been observed to increase in smaller halos (Giodini et al., 2009; Bahcall & Kulier, 2014). However, stars make up only a few percent of the total mass even in groups and the smallest clusters, and represent  $< 2\%$  of the total mass budget within  $r_{500}$  in rich clusters. Between ICM gas and stellar mass, there is not nearly enough to make up the total baryonic mass predicted from the cosmic baryon fraction.

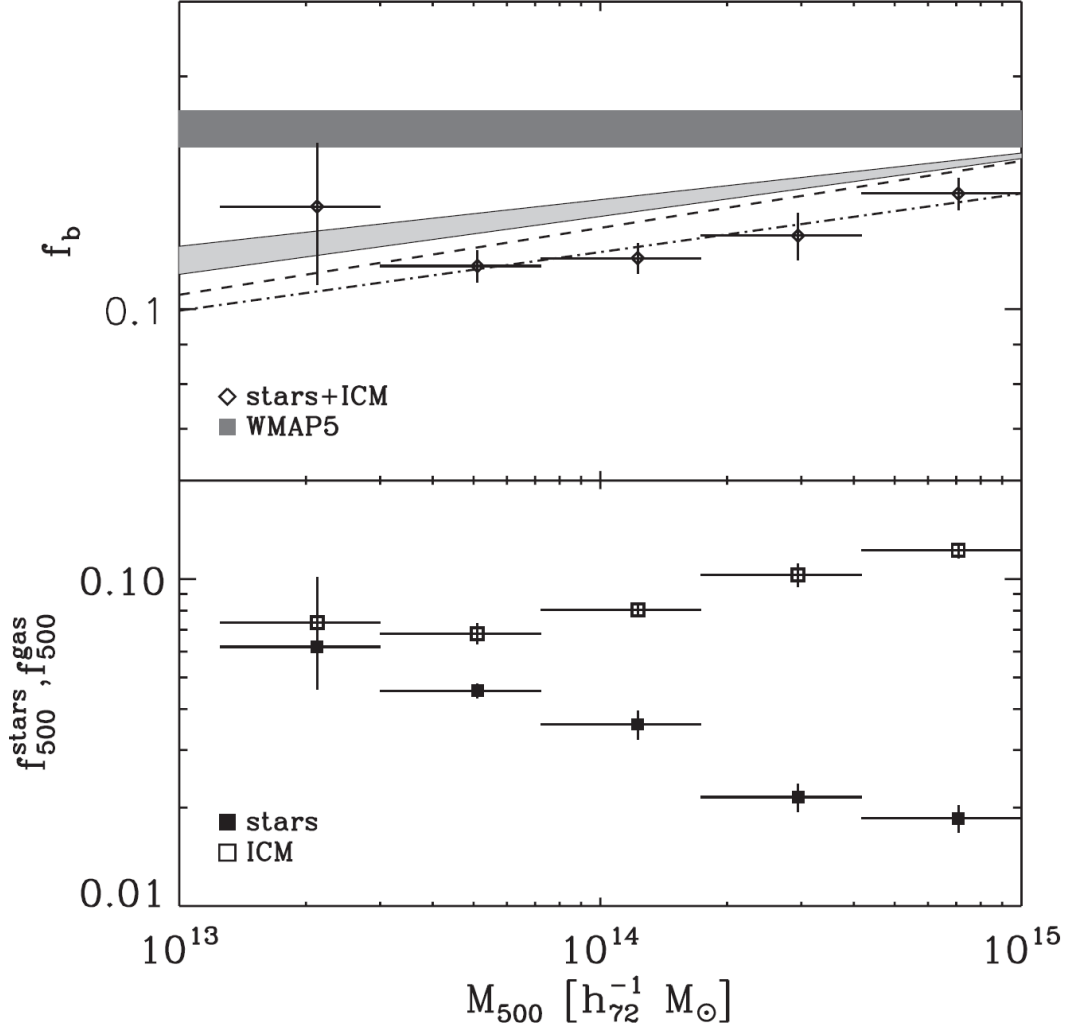


Figure 1.3: The problem of missing baryons, relative to halo mass, in groups and clusters. *Upper:* shows the total baryon fraction within  $r_{500}$  for groups and clusters binned by mass. The dark grey stripe represents the cosmic baryon fraction. All clusters are short of baryons, but low-mass halos are particularly deficient. *Lower:* the gas and stellar fractions of the halo bins. Figure from Giodini et al. (2009).

These discrepancies have been termed the “Missing Baryon Problem”, because observations have not been able to account for the expected abundance of baryons in galaxy clusters. The problem is more severe in smaller clusters, likely because baryons are less strongly bound to their shallow gravitational wells. Many attempts have been made to find a solution to this problem through theoretical and computational means. Possibly the most predominant such explanation is that additional non-gravitational energy is injected into the cluster, such as through shocks (Takizawa & Mineshige, 1998), preheating (Bialek et al., 2001), or a number of feedback mechanisms due to star formation or AGN activity (Metzler & Evrard, 1994; McCarthy et al., 2007; Bode et al., 2009). The net result of these additional energy sources is to extend the distribution of hot gas in the ICM, pushing more baryonic matter into the outskirts of the clusters while leaving the central regions devoid of gas and stars. These theories predict that more sensitive analysis of the outskirts of groups and clusters ( $\gtrsim r_{vir}$ ) should recover the missing gas mass left unaccounted for by observations of only the inner cluster regions. Rasheed et al. (2011) used extrapolations of observed gas density profiles to  $r_{vir}$ , corroborating the hypothesis that the missing gas mass is hidden in the cluster outskirts. Alternative theories predict that the missing baryons could be residing in additional phases, such as a cool diffuse gas phase, that have yet to be identified observationally (Afshordi et al., 2007; Bonamente et al., 2005).

## 1.4 The Galaxy-Halo Missing Baryon Problem

Galaxies form in dark matter halos of a range of sizes. Galaxies like the Milky Way and Andromeda (near the high-end of the galaxy mass range) are commonly referred to as  $L^*$  galaxies, and typically reside in halos with masses upwards of  $10^{12} M_{\odot}$  (Moster et al., 2010). The virial radii of these systems are around 300 kpc (Werk et al., 2014, and refs. therein). The baryonic components which dominate the

energy output in these halos (and are therefore the easiest to detect through emission) include the stellar disks, the gas and dust of the interstellar medium (ISM), and a hot, X-ray emitting halo of gas. Yet the most recent estimates of stellar mass in  $L^*$  galaxies (Behroozi et al., 2010) find that the stellar component makes up only  $\approx 5\%$  of the total mass, far less than anticipated if galactic halos also contain the cosmic baryon fraction. Including the cold ISM gas measured by HI surveys and the hot X-ray halo (Martin et al., 2010; Gupta et al., 2012, respectively) only increases the estimated baryon fraction in galaxies to around 8%. Therefore a similar “Missing Baryon Problem” is discussed in galactic halos because the disk cannot make up the entire anticipated baryon mass.

Several models have been developed which attempt to solve this “Galaxy-Halo Missing Baryon Problem,” through, for example, gas escaping galaxies through winds, jets, and outflows. Some theories predict unseen components in the intergalactic medium (IGM) which act as further reservoirs for baryons, but have yet to be accurately measured. These intergalactic components include a highly-photoionized Ly $\alpha$  forest (Sargent et al., 1980; Cen et al., 1994) or the warm-hot intergalactic medium (WHIM Cen & Ostriker, 1999; Dave et al., 1999). If galactic halos are indeed deficient of baryons, these IGM components must contain a higher proportion of baryons than expected from their disperse dark matter content.

Another reservoir for galactic baryons is a diffuse region of gas within the galactic halo itself, known as the circumgalactic medium (CGM Bahcall & Spitzer, 1969; Bergeron, 1985; Lanzetta et al., 1995), which may contain a large mass of baryons. Observational studies have begun to probe the CGM in the last few years through studies of QSO or galactic sightlines which pass through the CGM (Steidel et al., 2010; Prochaska et al., 2011; Tumlinson et al., 2011; Werk et al., 2013). When photons emitted by the background quasar or galaxy pass through the CGM, the gas (not energetic enough to be detected in emission) absorbs characteristic spectral lines from

the background spectrum, depending on the chemical makeup of the gas. The most common lines observed in absorption come from neutral hydrogen – hydrogen being the dominant source of baryonic mass in the universe. However, absorption from more highly-ionized species, such as Ca II (Zhu & Ménard, 2013), Mg II, Si II, C II, and O VI (Tumlinson et al., 2011; Werk et al., 2014), which are not significant contributors to baryonic mass, can be used to characterize the ionization state of the CGM gas. Knowledge of the ionization state can constrain the total hydrogen mass, including both neutral H I gas and the ionized H II. The observed metal-line absorption in QSO sightlines and the enrichment of the CGM also suggest that feedback effects are substantial in galaxy halos: metals created in the stellar disk are expelled into the outer regions of the halo, or even lost altogether, by feedback winds of  $\gtrsim 10^2$  km s $^{-1}$  (D’Odorico & Savaglio, 1991; Chen et al., 2010; Oppenheimer et al., 2012; Booth et al., 2012).

## 1.5 Our Investigation – Where are the Baryons?

In this thesis, we examine the most up-to-date observations available that can help solve the “Missing Baryon Problem”, and which address the overall distribution of baryons relative to dark matter. Generally, we wish to consider the questions: where are the baryons in dark matter halos of all sizes, how are they distributed, and what forms are they in?

Gas density profiles in clusters are observed to be shallower than the dark matter (NFW) profile, suggesting that there should be large reservoirs of baryons in the outskirts (e.g., Rasheed et al., 2011). We use published SZ and X-ray observations of cluster outskirts – along with extrapolations of the inner density profiles when necessary – to show that clusters *do contain the expected baryon fraction* in their halos; the baryons are less centrally concentrated than the dark matter, so that previous

observations of only the centers of clusters systematically missed the baryons.

Galaxy halos have significantly lower mass than cluster halos and their binding potential is lower, making it easier to expel baryons from the halo by feedback effects. Because of this, it is possible that the “Galaxy-Halo Missing Baryon Problem” is a consequence of a majority of baryons being removed from the halos altogether. However, the new observations of the CGM allow modernized constraints of the mass-content of the outer galactic halos. We study the distribution of baryons in galaxies using published absorption measurements of the CGM, and find they are consistent with the scenario that the *entire baryon fraction* can also be found within the virial radii of galaxies: a large fraction of the baryons simply reside in the hard-to-detect CGM.

Our investigation is organized as follows. In Chapter 2, we present the observations which constrain the baryonic mass within galaxy, group, and cluster halos. We also discuss the ways in which we extract predictions for the baryon fraction at the virial radius from extrapolations of measurements in the central regions. In Chapter 3, we show our results and compare the observed baryon fraction in halos to the cosmic baryon fraction derived from BBN and the CMB. We demonstrate that current evidence suggests that, averaged over sufficiently large scales, halos contain baryons in abundances consistent with the cosmic baryon fraction. This is observed in halos of a wide range of sizes, from galaxies to groups and clusters. In Chapter 4, we discuss the observational limitations and potential biases of our findings, compare them to simulations, and discuss the implications of our results. In Chapter 5, we present our conclusions on the subject of the baryonic mass distribution, and highlight future work that can be done to improve our findings.

Throughout this paper, we assume a cosmology of  $\Omega_m = 0.3$ ,  $\Omega_\Lambda = 0.7$ ,  $H_0 = 70 \text{ km s}^{-1} \text{ Mpc}^{-1}$  ( $h = 0.7$ ). Subscripts typically signify the value is evaluated within the indicated radius, such as  $f_{gas,500} = f_{gas}(< r_{500})$ .



# Chapter 2

## Observations and Data Analysis

### 2.1 Total Mass in Groups and Clusters

The total mass in groups and clusters can be measured in a number of ways. The most direct method of calculating the mass profile of a large halo is through gravitational lensing of the light of background sources behind the halo. Strong gravitational lensing occurs when the background object (e.g., a high-redshift galaxy) is magnified and severely warped by the gravitational potential of the lens (foreground cluster). This allows a very accurate measurement of the mass of the lens, but occurs only rarely when the background/foreground are in a particular alignment. More commonly utilized is the technique of weak gravitational lensing (e.g., Umetsu et al., 2009; Sheldon et al., 2009a; von der Linden et al., 2014), where small distortions of an immense number of background objects are used to statistically determine the mass profile of a foreground halo.

Another common method of estimating the mass of groups and clusters is through the assumption of *hydrostatic equilibrium* (HSE). If the gas in clusters is in hydrostatic

equilibrium, then the pressure gradient offsets the gravitational force:

$$\frac{dP(r)}{dr} = -\frac{G M(< r) \rho_{gas}(r)}{r^2} \quad (2.1)$$

Therefore, assuming the ICM is in hydrostatic equilibrium, the total mass profile can be reconstructed from the observed gas density and pressure profiles:

$$M(< r) = -\frac{r^2}{G \rho_{gas}(r)} \frac{dP(< r)}{dr} . \quad (2.2)$$

Alternatively, the total mass can be calculated using the density and temperature profiles, assuming the ICM behaves as an ideal gas,  $P(r) = n(r)kT(r)$ :

$$M(< r) = -\frac{k T(r) r}{G} \left( \frac{d \log \rho_{gas}(r)}{dr} + \frac{d \log T(r)}{dr} \right) . \quad (2.3)$$

Gas density is typically measured using X-ray observations, as the gas density is easily calculated from the X-ray surface brightness. Temperature can be determined from X-ray spectroscopy, and pressure can be measured directly through the thermal SZ effect.

Whether the total mass derived through the assumption of hydrostatic equilibrium (or the “hydrostatic mass”) is biased relative to the true mass is highly debated, as sources of non-thermal pressure (including cosmic rays, merger-induced shocks, and AGN feedback) can invalidate the assumption of hydrostatic equilibrium. Comparing hydrostatic masses to masses derived through weak lensing analysis can help constrain the bias inherent in the HSE assumption. In Section 4.1.1, we discuss observational and theoretical constraints on the hydrostatic mass bias.

The total matter density distribution is often modeled by the NFW profile, an analytic equation first proposed by Navarro et al. (1996) to describe the “universal density profile” of simulated dark matter halos, regardless of size. The NFW profile

has the form:

$$\rho_m(r) = \frac{\delta_c \rho_{crit}}{(r/r_s)(1 + r/r_s)^2} . \quad (2.4)$$

$r_s$  is a characteristic radius representing the central core of the dark matter halo,  $\rho_{crit}$  is the critical matter density, and  $\delta_c$  is a normalization constant which sets the characteristic overdensity of the cluster. Halos which fit the NFW profile are self-similar, in that  $r_s$  and  $\delta_c$  are determined uniquely by the total halo mass. When  $r \lesssim r_s$ , the density profile decreases slowly ( $\rho_m \propto r^{-1}$ ), while at  $r \gg r_s$  the profile steepens significantly ( $\rho_m \propto r^{-3}$ ). Observations of group and cluster halos consistently find that the total mass profile follows the NFW profile well (e.g., Vikhlinin et al., 2006; Mandelbaum et al., 2008; Sheldon et al., 2009a; Umetsu et al., 2009).

Several “mass proxies” have been used to estimate the total mass of clusters. Mass proxies are typically easily-observed quantities that are found to correlate strongly with the total cluster mass. Examples include the X-ray temperature ( $kT_X \approx 1 - 10$  keV for groups and clusters), the richness (number of bright galaxies observed within the cluster), the X-ray luminosity, and  $Y_X = M_{gas} T_X$ . Using mass proxies allows observers to place loose constraints on the mass of a cluster without requiring deep observations to recover the true gas or mass density profiles. The assumption of hydrostatic equilibrium can also affect the determination of mass through this method, as many Mass-Proxy relations are calibrated against hydrostatic masses of clusters (e.g., Arnaud et al., 2007, 2010).

## 2.2 Cluster Gas Mass Fraction

The baryonic content of galaxy groups and clusters is dominated by hot plasma in the intracluster medium (ICM). Until very recently, the most sensitive X-ray and SZ observations were only able to constrain the gas mass in the ICM in the inner regions of groups and clusters, typically to around  $r_{500}$  (e.g., Vikhlinin et al., 2006; Arnaud

et al., 2007; Sun et al., 2009). Because  $r_{vir}$  is about twice  $r_{500}$ , these observations only probe the inner  $\approx 1/8$  of the virial volume of group and cluster halos. In order to measure the baryon distribution within the entire halo of groups and clusters, it is essential to consider the gas within a volume substantially larger than that within  $r_{500}$ . Here, we describe the relevant observations of groups and clusters which measure both the ICM and total mass of the dark matter halo. Because very few observations retain the sensitivity required to measure the gas density in the outskirts of clusters, we also discuss a method of using measured gas density profiles to extrapolate observed gas fractions to higher radii.

### 2.2.1 Observations

**Vikhlinin et al. (2006)** derived the gas and total mass profiles of 10 low-redshift (median redshift  $z = 0.06$ ) relaxed clusters using long-exposure *Chandra* observations. The clusters have a median mass  $M_{vir} = 7.3 \times 10^{14} M_{\odot}$ , and range from  $M_{vir} = 1.1 \times 10^{14} - 1.5 \times 10^{15} M_{\odot}$ . Temperatures range from  $kT = 2 - 9$  keV. The authors measured X-ray temperature and surface brightness profiles to approximately  $r_{500}$ . They modeled the surface brightness profile (which is proportional to  $n_e n_p$ ) to recover the gas particle density,  $\rho_{gas}(r)$ . The total mass ( $M_{500}$ ) was calculated by solving the equation of hydrostatic equilibrium, using the observed density and temperature profiles, and is well-fit by an NFW profile in most cases. The integrated gas density and total mass profiles were used to derive the gas fraction interior to  $r_{500}$ ,  $f_{gas,500}$ . This gas fraction ranges widely from cluster to cluster, from 6% to 14%, with median 11%. These observations were also used to derive a useful scaling relation between  $M_{500}$  and the X-ray temperature  $T$ :

$$M_{500} = (2.97 \pm 0.15) \times 10^{14} M_{\odot} h_{70}^{-1} \left( \frac{T}{5 \text{ keV}} \right)^{1.58 \pm 0.11}. \quad (2.5)$$

**Arnaud et al. (2007)** used very similar methods to derive the gas and total mass profiles of 10 low-redshift (median  $z = 0.09$ ) relaxed clusters from *XMM-Newton* observations. The clusters range in mass from  $M_{vir} = 1.2 \times 10^{14} - 1.16 \times 10^{15} M_{\odot}$ , with a median of  $4.2 \times 10^{14} M_{\odot}$ , and temperatures vary from  $kT = 2 - 8$  keV. The total mass also relies on the assumption of hydrostatic equilibrium, and was extrapolated from  $\approx r_{700}$  to  $r_{500}$  using an NFW profile.  $f_{gas}$  was derived out to  $r_{500}$  for these clusters, varying from 5.5% to 16%, with median 11%, similar to the Vikhlinin et al. (2006) measurements.

**Sun et al. (2009)** analyzed the gas fraction in 43 groups from archival *Chandra* observations. All the groups are at low redshifts ( $z \lesssim 0.1$ ). Of these 43 observations, 11 were sensitive enough to measure the X-ray surface brightness to  $r_{500}$ , while an additional 12 measured surface brightness to  $r_{1000}$  and were extrapolated to  $r_{500}$ . The total mass of the 23 best-measured groups ranges from  $M_{vir} = 2.0 \times 10^{13} - 2.1 \times 10^{14} M_{\odot}$ , with a median of  $1.1 \times 10^{14} M_{\odot}$ , and ICM temperatures range from  $kT = 0.7 - 2.7$  keV. The total mass (assuming hydrostatic equilibrium) and gas mass were calculated using similar principles to Vikhlinin et al. (2006), with errors estimated by using 1000 artificial profiles generated from Monte-Carlo simulations.  $f_{gas,500}$  for these 23 groups ranges from 5% – 11%, with a median of 8%, lower than for the more massive clusters of Vikhlinin et al. (2006) and Arnaud et al. (2007).

The above three samples were combined in the analysis of **Giodini et al. (2009)** (G09), which used all 10 clusters from Vikhlinin et al. (2006), all 10 clusters from Arnaud et al. (2007), and 21 of the 23 best-measured groups from Sun et al. (2009) to study the group/cluster gas mass fraction over a wide range of halo masses. The authors binned the 41 groups and clusters logarithmically by mass, highlighting that lower mass halos have significantly lower gas fractions. The best-fit trend is:

$$f_{gas}(< r_{500}) = (9.3 \pm 0.2) \times 10^{-2} h_{70}^{-3/2} \left( \frac{M_{500}}{2 \times 10^{14} M_{\odot}} \right)^{0.21 \pm 0.03}. \quad (2.6)$$

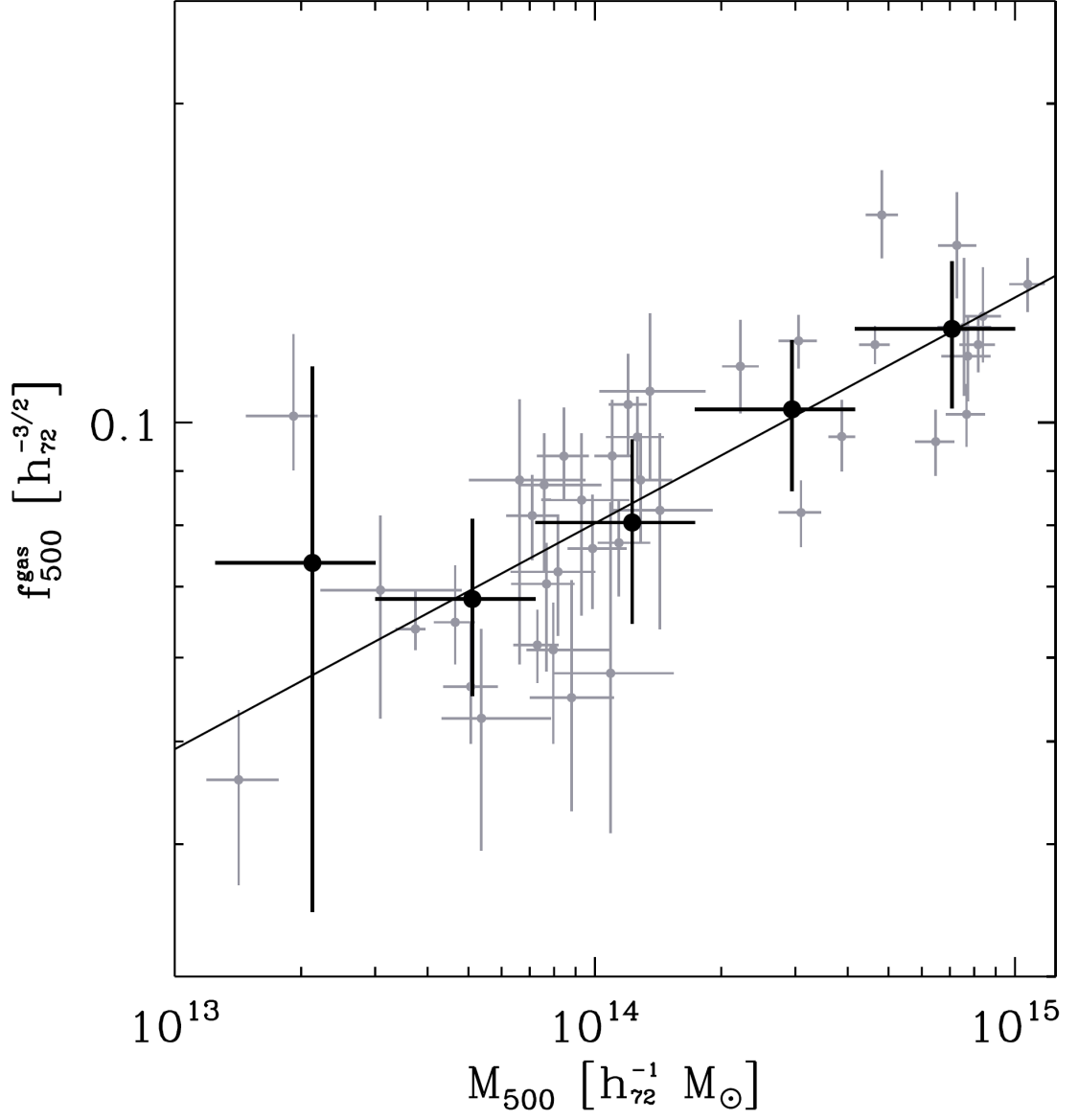


Figure 2.1: The dependence of  $f_{gas}(< r_{500})$  on  $M_{500}$  ( $\approx 0.73M_{vir}$ ), as presented in Giodini et al. (2009). The light-grey points represent individual group/cluster observations from Vikhlinin et al. (2006), Arnaud et al. (2007), and Sun et al. (2009), while the dark points are the average gas fractions, binned logarithmically with mass. Lower-mass halos show significantly lower gas fractions, with  $f_{gas}(< r_{500})$  scaling roughly as  $M_{500}^{0.21}$ .

Figure 2.1 shows the distribution of the observed gas fractions, as a function of halo mass, measured by the three works above. We will use the G09 bins as 5 independent samples of  $f_{gas}$  for different masses.

Recent results from the *Planck* satellite detected the ICM using the thermal SZ effect, which measures the integrated line-of-sight gas pressure. **Planck Collaboration (2013d)** (hereafter PC13) derived a stacked pressure profile for 62 massive clusters that have archival observations with *XMM-Newton*. The cluster sample (detailed in Planck Collaboration, 2011) includes clusters of mass  $M_{vir} = 3.3 \times 10^{14} - 2.7 \times 10^{15} M_{\odot}$ , with median mass approximately  $M_{vir} = 8.70 \times 10^{14} M_{\odot}$ . X-ray temperatures range from  $kT = 3.4 - 13$  keV. Total mass ( $M_{500}$ ) was derived from a scaling relation with the quantity  $Y_X = M_{gas} T_X$ , an observable quantity that has been found to be a good mass proxy. The scaling relation in question (Arnaud et al., 2010) was calibrated against X-ray derived hydrostatic masses, and so the total mass of the stacked *Planck* clusters assumes hydrostatic equilibrium. The total mass beyond  $r_{500}$  was calculated assuming an NFW profile. The stacked pressure profile is measured to unprecedented scales ( $3r_{500} \approx 1.6r_{vir}$ ), although the X-ray temperature profile measured by *XMM-Newton* only extends to  $r_{500}$ , so the authors extrapolated the observed temperature profile to  $3r_{500}$  to match the pressure observations.

Assuming the ICM acts as an ideal gas ( $P = n_e kT$ ), the authors inverted the pressure and temperature profiles to retrieve the gas density profile and derive  $f_{gas}(< r)$  out to  $3r_{500}$ <sup>1</sup>. The reconstruction of the temperature profile was initially flawed, and the correct gas fraction profile was given in an erratum, Planck Collaboration (2013c). The gas fraction increases from  $r_{500}$  to  $r_{vir}$  (as predicted by Rasheed et al., 2011, see 2.2.2), reaching a peak of  $\approx 15 \pm 2\%$  at  $1.6r_{vir}$ .

**Eckert et al. (2013a)** (E13) combined the stacked pressure profile from Planck Collaboration (2013d) with a stacked X-ray surface-brightness profile that directly

---

<sup>1</sup>The authors also derive the gas fraction assuming a conservative case in which the ICM is isothermal beyond  $r_{500}$ , resulting in lower  $f_{gas}$ .

constrains the gas density to  $r_{200}$ . The X-ray observations were performed with *ROSAT*, on a sample of 31 clusters ( $z \lesssim 0.2$ ) of temperatures  $kT = 2.5 - 9$  keV, with median  $kT = 6.5$  keV. The cluster masses range from  $M_{vir} \approx 1.4 \times 10^{14}$  to  $1.0 \times 10^{15} M_{\odot}$ , with median  $M_{vir} = 6.0 \times 10^{14} M_{\odot}$ <sup>2</sup>. The *Planck* pressure profile, combined with the gas density profile, was used to calculate the total mass, assuming hydrostatic equilibrium. This is different from the method used by Planck Collaboration (2013d), which used a scaling relation and assumed an NFW profile. However, both estimates rely on the assumption of hydrostatic equilibrium either explicitly or implicitly through calibration of the  $Y_X - M_{500}$  relation. 18 clusters are in common between the *ROSAT* and *Planck* samples, and the authors separated them into cool-core (CC, 6 clusters) and non-cool core (NCC, 12 clusters) categories. The gas fraction profile was calculated separately for the two categories, and the authors found that NCC clusters have significantly higher gas fractions within  $r_{200}$  ( $0.169 \pm 0.010$ ) than relaxed, CC clusters do ( $0.134 \pm 0.011$ ), suggesting that the irregular, non-spherical morphologies of the disturbed clusters may bias the gas fractions high. They also found that  $f_{gas}$  increases from  $r_{500}$  to  $r_{200}$  ( $f_{gas,500} \approx 0.12$  for CC clusters).

**Umetsu et al. (2009)** (U09) observed the ICM of four very massive ( $M_{vir} \gtrsim 1 \times 10^{15} M_{\odot}$ ,  $kT \approx 9 - 10$  keV) clusters using Thermal SZ measurements with the *AMiBA* CMB telescope. After deriving pressure profiles from the SZ effect, the authors calculated the gas density profile using archival X-ray temperature measurements and a theoretically-derived temperature profile (Komatsu & Seljak, 2001). The authors use *Subaru* observations to derive the cluster masses with weak lensing analysis. The average gas fraction is calculated to the limit of the SZ observations,  $r_{200}$ , and is found to be  $f_{gas}(< r_{500}) = 0.126 \pm 0.019$  within  $r_{500}$  and  $f_{gas}(< r_{200}) = 0.133 \pm 0.020$  within  $r_{200}$ . These observations also find that  $f_{gas}$  increases with radius beyond  $r_{500}$ , in agreement with Planck Collaboration (2013d) and Eckert et al. (2013a). We em-

---

<sup>2</sup>The authors do not give the masses of the clusters, so these values are taken from the  $M - T$  relation of Vikhlinin et al. (2006) (our equation 2.5).



phasize that the total mass for these clusters is *not* dependent on the assumption of hydrostatic equilibrium (because they were derived using weak lensing measurements). See our discussion of the hydrostatic mass bias in Section 4.1.1.

Table 2.1 lists the observed data from the samples described above, including the most important characteristics of each sample: median mass ( $M_{vir}$ ), whether that mass is derived assuming HSE, and the gas fraction at directly-observed radii.

Table 2.1: Samples of Groups/Clusters: Relevant Observations

Reference (1)	Clusters (2)	$\langle M_{vir} \rangle (M_{\odot})$ (3)	HSE? (4)	$f_{gas,500}$ (5)	$f_{gas,200}$ (6)	$f_{gas,vir}$ (7)
G09 Bin 1	2	$2.9 \times 10^{13}$	✓	$0.074 \pm 0.028$		
Bin 2	7	$7.0 \times 10^{13}$	✓	$0.068 \pm 0.005$		
Bin 3	17	$1.7 \times 10^{14}$	✓	$0.080 \pm 0.003$		
Bin 4	5	$4.1 \times 10^{14}$	✓	$0.103 \pm 0.008$		
Bin 5	10	$9.8 \times 10^{14}$	✓	$0.123 \pm 0.007$		
PC13	62	$8.7 \times 10^{14}$	✓	$0.125 \pm 0.005$	$0.137 \pm 0.003$	$0.145 \pm 0.01$
E13 - CC	6	$5.9 \times 10^{14}$	✓	$0.115 \pm 0.010$	$0.134 \pm 0.011$	
U09	4	$1.2 \times 10^{15}$		$0.126 \pm 0.019$	$0.133 \pm 0.020$	

(1) G09, PC13, E13, and U09 stand for Giodini et al. (2009), Planck Collaboration (2013d), Eckert et al. (2013a), and Umetsu et al. (2009), respectively. CC represents the sub-sample of cool-core clusters.

(2) The number of clusters in each sample. (3) The median virial mass of the clusters.

(4) ✓ marks that the total mass assumes hydrostatic equilibrium.

(5)  $f_{gas}(< r_{500})$  (6)  $f_{gas}(< r_{200})$  (7)  $f_{gas}(< r_{vir})$

## 2.2.2 Extrapolation of Gas Density Profiles

As seen above, very few observations retain the sensitivity necessary to measure the gas density all the way to  $r_{vir}$ . Therefore, to constrain the gas fraction within the entire halo, we extrapolate the observed gas mass profile (at  $r_{200}$  or  $r_{500}$ ) to higher radius by assuming a power-law profile:

$$\rho_{gas}(r) \propto r^{-\alpha_{gas}}, \quad (2.7)$$

where  $\alpha_{gas}$  is the slope of the gas density profile, which can in general change as radius increases. The total matter density can be similarly modeled,

$$\rho_m(r) \propto (r)^{-\alpha_m} , \quad (2.8)$$

with  $\alpha_m$  the slope of the total mass density profile. At large radii, the full equation for the gas fraction simplifies to approximately:

$$\begin{aligned} f_{gas}(< r) &= \frac{M_{gas}}{M_{tot}} = \frac{\int_0^r 4\pi r'^2 \rho_{gas}(r') dr'}{\int_0^r 4\pi r'^2 \rho_m(r') dr'} \\ &\approx \frac{\rho_{gas}(r)}{\rho_{tot}(r)} \\ &\propto r^{\alpha_m - \alpha_{tot}} . \end{aligned} \quad (2.9) \quad (2.10)$$

Therefore, the gas fraction can be extrapolated to larger radii using the difference in slopes between the gas density and total mass density profiles.

**Rasheed et al. (2011)** (R11) used this approach to extrapolate the gas fraction of the G09 cluster samples to  $r_{vir}$ . X-ray and SZ observations show that the gas density decreases more slowly with radius than the total mass density ( $\alpha_{gas} < \alpha_m$ ), suggesting that the gas fraction should increase when the cluster outskirts are considered. The authors hoped to place constraints on the amount of “missing baryons” within the virial volume of clusters.

R11 surveyed the literature to recover X-ray measurements which constrain the gas density slope out to  $r_{500}$ . These measurements include observations with *ROSAT*, *Chandra*, *XMM-Newton*, and *Suzaku*, and cover a wide range of cluster masses and temperatures. Averaging over the many observations, the authors find that the gas density slope at  $r_{500}$  is steeper in with more massive clusters, with  $\alpha_{gas}$  ranging from  $\approx 1.8 \pm 0.2$  for poor clusters (G09 bin 2,  $M_{vir} \approx 7 \times 10^{13} M_\odot$ ) to  $\approx 2.3 \pm 0.02$  for the most massive G09 bin ( $M_{vir} \approx 9.8 \times 10^{14} M_\odot$ ).

Compared to the gas density profile, the total density (NFW) profile is significantly steeper in the outer regions of the halo. The NFW profile has a slope of  $\alpha_m = 2.6$  between  $r_{500}$  and  $r_{200}$ , and steepens to  $\alpha_m = 2.7$  in the region  $r_{200}$  to  $r_{vir}$ . Therefore, R11 predicted that the gas fraction rises significantly above  $r_{500}$ . Because  $\alpha_{gas}$  increases with cluster mass, the gas fraction is predicted to rise more quickly with radius in groups and poor clusters ( $f_{gas} \propto r^{0.8}$  for G09 bin 2) than in rich clusters ( $f_{gas} \propto r^{0.3}$  for G09 bin 5). For these two bins, this model predicts increases in  $f_{gas}$  by a factor of roughly 1.6 and 1.2, respectively, from  $r_{500}$  to  $r_{vir}$ . This offers an explanation for the particular deficiency of baryons in low-mass clusters: the shallower gas profile implies the ICM is less centrally-concentrated than in massive clusters, and the gas is extended further into the cluster outskirts.

We adopt R11's extrapolation model in order to approximate the gas fraction at high radius in the samples which do not measure  $f_{gas}$  to  $r_{vir}$  (all except PC13).  $\alpha_{gas}$  for each sample in Table 2.1 is taken from the temperature-slope relation in R11; for consistency, we do not extrapolate the gas profiles for any individual cluster sample with coverage beyond  $r_{500}$ . We assume  $\alpha_m$  as above for the NFW profile ( $\alpha_m = 2.6$  for  $r < r_{200}$ , 2.7 for  $r > r_{200}$ ). We extrapolate  $f_{gas}$  from the maximum observed radius,  $r_a$ , to a larger radius  $r_b$  using:

$$f_{gas,b} = f_{gas,a} \left( \frac{r_b}{r_a} \right)^{\alpha_m - \alpha_{gas}}. \quad (2.11)$$

For example, extrapolating the gas fraction of G09's bin 5 from  $r_{500}$  to  $r_{200}$ :

$$\begin{aligned} f_{gas,200} &= f_{gas,500} \left( \frac{r_{200}}{r_{500}} \right)^{\alpha_m - \alpha_{gas}} \\ &\approx 0.103 (1.45)^{2.6-2.3} \\ &\approx 0.115 \end{aligned} \quad (2.12)$$

To calculate the uncertainty on the extrapolated gas fraction, we propagate the errors in  $f_{gas,a}$  and in  $\alpha_{gas}$ , making the simplification that no significant uncertainty exists in  $\alpha_m$  or  $r_b/r_a$ . The fractional errors add in quadrature.

$$\frac{\Delta f_{gas,b}}{f_{gas,b}} = \sqrt{\left(\frac{\Delta f_{gas,a}}{f_{gas,a}}\right)^2 + \left(\frac{\Delta (r_b/r_a)^{\alpha_m - \alpha_{gas}}}{(r_b/r_a)^{\alpha_m - \alpha_{gas}}}\right)^2}. \quad (2.13)$$

The uncertainty in the right term is

$$\Delta (r_b/r_a)^{\alpha_m - \alpha_{gas}} = (r_b/r_a)^{\alpha_m - \alpha_{gas}} \ln(r_b/r_a) \Delta \alpha_{gas}, \quad (2.14)$$

yielding the final result:

$$\frac{\Delta f_{gas,b}}{f_{gas,b}} = \sqrt{\left(\frac{\Delta f_{gas,a}}{f_{gas,a}}\right)^2 + (\ln(r_b/r_a) \Delta \alpha_{gas})^2}. \quad (2.15)$$

The gas density profile is expected to steepen at very large radii, such that it eventually matches the NFW profile (e.g., Umetsu et al., 2009), which translates to the gas fraction asymptotically approaching a constant value. At large enough radius, extrapolation of the gas fraction as described above will, therefore, become invalid, as  $\alpha_{gas}$  will not remain fixed. The range at which the gas density steepens significantly is not known, however, as observational data does not currently constrain  $\alpha_{gas}$  far beyond  $r_{500}$ . R11's assumption that this slope remains constant to  $r_{vir}$  is therefore a questionable one, but no simple alternatives exist. We, likewise, assume  $\alpha_{gas}$  remains constant to  $r_{vir}$  (and slightly beyond), and emphasize that our calculation of the gas fraction will be biased high if the gas density slope steepens significantly beyond  $r_{500}$ . In Section 4.1.3, we discuss current constraints on this steepening of this slope.

## 2.3 Cluster Stellar Mass Fraction

The integrated stellar mass of groups and clusters is also an important (although subdominant) reservoir of baryons in these large halos. The stellar mass of clusters is thought to come almost entirely from the stellar content of the individual cluster galaxies.

G09 approximated the stellar content of a large number ( $> 90$ ) of groups and clusters from the *COSMOS* survey. Using optical and infrared observations from *Subaru*, the authors fit a broad-band spectrum to the detected galaxies in each cluster and used these spectral energy distributions to derive photometric redshifts for the sample. Converting the *Ks*-band (IR) luminosity of detected galaxies to stellar mass, and accounting for the entire predicted galactic mass function, G09 approximated the stellar fraction in clusters of sizes  $1 \times 10^{13} - 1 \times 10^{15} M_{\odot}$ . At  $r_{500}$ , the stellar fraction was found to be significantly higher ( $\approx 6\%$ ) for groups and poor clusters than for the most massive clusters ( $\approx 2\%$ ). The authors derived a fit to stellar-fraction versus mass of:

$$f_*( < r_{500} ) = (5.0 \pm 0.1) \times 10^{-2} \left( \frac{M_{500}}{5 \times 10^{13} M_{\odot}} \right)^{-0.37 \pm 0.04}. \quad (2.16)$$

The results of an extensive Sloan Digital Sky Survey (SDSS) weak lensing study of stacked groups and clusters has placed unparalleled constraints on the stellar fraction in clusters. The MaxBCG sample (Sheldon et al., 2009a) contains  $> 130,000$  clusters between redshifts  $z = 0.1 - 0.3$ . Sheldon et al. (2009b) binned the clusters by richness and luminosity, and stacked by centering on the brightest cluster galaxy (BCG). The mean weak lensing profile was detected well into the surrounding large scale structure ( $\gtrsim 15 - 20 r_{vir}$ ), as was the averaged optical surface brightness, allowing the total mass to light ratio (M/L) to be calculated. **Bahcall & Kulier (2014)** (BK14) developed a model for the stellar mass to light ratio of individual spiral and elliptical galaxies, as well as their relative abundance from the density-morphology relation, and converted

the total mass to light ratio into the stellar mass fraction.

Figure 2.2 shows the stellar fraction distributions derived by BK14. The stellar fraction is calculated at  $r_{200b}$ <sup>3</sup> as a function of cluster mass. The authors find that the stellar fraction at this fixed radius decreases with halo mass, in excellent agreement with G09. The stellar fraction is also calculated as a function of radius, divided into three richness bins, with mass ranges corresponding roughly to  $M_{vir} < 2 \times 10^{13} M_\odot$ ,  $2 \times 10^{13} M_\odot < M_{vir} < 1 \times 10^{14} M_\odot$ , and  $M_{vir} > 1 \times 10^{14} M_\odot$ . The stellar fraction decreases significantly from the centers of clusters (where the light is dominated by the BCG), asymptotically approaching at high radius a “cosmic stellar fraction” of  $f_* \approx 0.01 \pm 0.004$  in all richness bins. The radius at which the stellar fraction reaches this cosmic limit decreases with richness class, suggesting that all clusters contain roughly the same stellar fraction, but that the stellar mass distribution is more extended in low-mass clusters with shallow gravitational potentials.

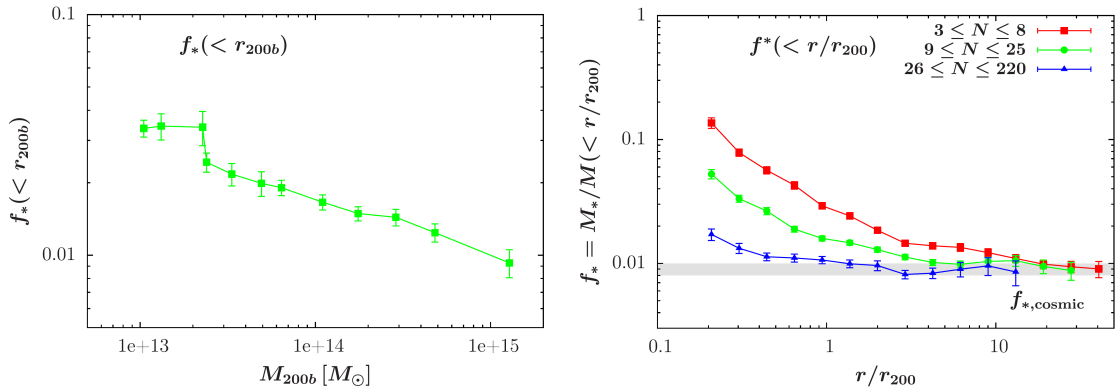


Figure 2.2: The stellar fraction from stacked optical and weak lensing observations, as presented in Bahcall & Kulier (2014). *Left*: The stellar fraction within  $r_{200b} \approx r_{vir}$  in groups and clusters, as a function of total mass.  $f_*$  decreases in more massive clusters, in agreement with observations collected by Giodini et al. (2009). *Right*: The stellar fraction as a function of halo-centric radius. The profiles are binned by richness, a proxy for mass. More massive clusters have lower stellar fraction at any given radius (lower mass halos are more dominated by their BCGs), but the stellar fraction tends towards a constant value at high radius irrespective of mass: the “cosmic stellar fraction”  $\approx 1\%$ .

<sup>3</sup> $r_{200b}$  represents where the density is 200 times the cosmic matter density, not the critical density, and corresponds roughly to our definition of  $r_{vir}$ .

## 2.4 Galaxy Mass Fractions

Studying the distribution of baryons in individual galaxies presents many other challenges not faced in the investigation of clusters. Because galaxy halos are significantly lower mass than cluster halos ( $M_{vir} \approx 1 - 2 \times 10^{12} M_{\odot}$  for a typical  $L^*$  galaxy), their gravitational wells are shallower, and it is easier for feedback effects to remove gas from the systems altogether (e.g., Oppenheimer et al., 2010). The lower total mass also translates to a much lower thermal temperature for the gas to be in hydrostatic equilibrium. Therefore, the main diffuse gaseous component of galaxy halos will primarily be too cool and low density to be detected in emission.

The most obvious and easily detected baryon reservoir in ( $L^*$ ) galaxy halos is the galactic disk itself, which contains the stellar population as well as the gas and dust of the ISM. Baryons are also stored in the “circumgalactic medium” (CGM), a large, diffuse region surrounding galaxies with low temperatures and densities. Observations are beginning, for the first time, to place reasonable constraints on the total mass in this baryonic phase, allowing estimates of the makeup, distribution, and total fraction of baryons in the low-mass halos of galaxies.

### 2.4.1 The Circumgalactic Medium

The existence of the CGM was first predicted by Bahcall & Spitzer (1969) to explain the presence of absorption features in the spectra of quasars. The emission from quasars was known to come from high redshift, while the absorption lines came from lower redshifts (typically  $z = 1 - 3$ ), had low dispersion velocities, and showed the presence of many abundant elements and ionization states (including absorption from H I, C II, C IV, Si II, and many others). The authors predicted that an extended halo of gas ( $r \approx 10^2$  kpc) surrounding normal galaxies ( $M \approx 10^{11} - 10^{12} M_{\odot}$ ) could produce the observed absorption profiles and dispersion velocities. Even at this early stage,

many separate phases of the CGM were predicted, as temperatures ranging from  $2 \times 10^4 - 2 \times 10^5$  K were required to explain the variety of ionization states.

Subsequent observations have confirmed this hypothesis by associating the absorption features in QSO sightlines to nearby foreground galaxies with the expected redshifts. The CGM is a gaseous reservoir in the dark matter halo around galaxies, which extends for several hundred kiloparsecs, and likely as far as the virial radius ( $r_{vir} \approx 300$  kpc for an  $L^*$  galaxy). The CGM is also likely the major source of pristine gas accreting onto the galactic disk.

The use of QSO and galaxy absorption spectroscopy remains the most powerful tool in statistically characterizing the CGM. The high spatial density of background galaxies and quasars results in a large number of sightlines through the CGM at a wide variety of projected distances. While it is very unlikely to have enough bright background sources to resolve the distribution of the CGM in any individual galaxy, it is possible to recover the average profile of gas absorption in many galaxies as a function of radius by stacking many sightlines together by the projected distance from their absorbing galaxy.

Steidel et al. (2010) used a sample of 512 galaxy pairs, where both foreground and background galaxies have spectroscopic redshifts and are separated by less than  $15''$  on the sky. At the median redshift of the foreground absorbers ( $z \approx 2$ ), this translates to projected distances within 125 kpc. Absorption profiles (stacked into three projected radius bins) were measured for  $\text{Ly}\alpha$ , C IV (1549Å), C II (1334Å), Si IV (1393Å), and Si II (1260Å and 1526Å). Hydrogen, the most dominant element by mass in the CGM, is measured in its neutral phase through  $\text{Ly}\alpha$  absorption, and is observed well beyond 100 kpc. Using an approximate model for populating the CGM by galactic outflows, the authors place a rough constraint on the CGM mass of  $M_{CGM} \approx 3 \times 10^{10} M_{\odot}$ . By this approximation, the CGM contains roughly the same mass content as the sum of stars and gas in the stellar disk, and amounts to  $\approx 3 - 4\%$  of the total mass of the



dark matter halo ( $\approx 20\%$  of the expected baryonic mass, assuming the halo contains the entire cosmic baryon fraction).

The COS-Halos survey (Tumlinson et al., 2011) was designed specifically to study the CGM in low-redshift galaxies. It uses far-UV spectroscopy of background quasars behind 44 roughly  $L^*$  galaxy halos, observed with the Cosmic Origins Spectrograph instrument on the Hubble Space Telescope. Measuring the column density in  $\text{Ly}\alpha$ , early results (Thom et al., 2012; Werk et al., 2013) placed a very conservative lower limit on the CGM gas mass of  $M_{\text{CGM}} > 10^9 M_\odot$ . Later analysis by **Werk et al. (2014)** (W14) developed a model for the ionization state of the CGM, constrained by the observed absorption of low, intermediate, and high-ionization transitions in metals. This model – which indicates that the hydrogen in the CGM is increasingly ionized at higher radii – is used to greatly improve the limits on the CGM mass. Integrating their best-fit gas density profile to the virial radius (300 kpc), they find that the cool phase ( $T \approx 10^4 - 10^5$  K) of the CGM in  $L^*$  galaxies has a mass of  $M_{\text{CGM}} \approx 9.5 \times 10^{10} M_\odot$ . This CGM mass is consistent with the rough estimate made by Steidel et al. (2010), and is similar to the combined mass of the stellar disk and ISM. The uncertainty in  $M_{\text{CGM}}$  is dominated by saturation in a few  $\text{Ly}\alpha$  absorption profiles. The minimum CGM mass is  $M_{\text{CGM}} > 6.5 \times 10^{10} M_\odot$ , and could range as high as  $M_{\text{CGM}} \approx 1.2 \times 10^{11} M_\odot$  if all saturated column densities are 3 times higher than their lower limits. The total halo mass of  $L^*$  galaxies is approximately  $1.6 \times 10^{12} M_\odot$ , so the authors conclude the CGM accounts for 25 – 45% of the expected baryonic mass in galaxies ( $M_b = f_{b,\text{cosmic}} M_{\text{vir}} \approx 2.6 \times 10^{11} M_\odot$ ).

### 2.4.2 Estimate of The Galactic Halo Baryon Fraction

W14 combined their estimate of the cool gas mass in the CGM with observations of other baryonic components of galactic halos to constrain the total baryon fraction currently detected within the virial radius. The median stellar mass of the COS-Halos

galaxies is  $\langle M_* \rangle = 4 \times 10^{10} M_\odot$ , in agreement with abundance matching estimates (Behroozi et al., 2010). The gaseous component of the ISM, observed with HI surveys, can vary from very little (for elliptical galaxies) to of order the stellar mass (McGaugh et al., 2010; Martin et al., 2010). Together, for a star-forming  $L^*$  galaxy, the mass of the stellar and gaseous disk (the normal galactic component) is given as  $7 \times 10^{10} M_\odot$ . Thus, the disk contributes about 4 – 5% of the total mass of the galactic halo, or about 27% of the expected baryon content.

The presence of high-ionization absorption lines in CGM profiles suggests that a warm ( $> 10^5$  K) CGM component exists. The ionization model derived by W14 to fit the low-ionization transition abundances severely underestimates the column density of O VI. The authors reference halo models which predict a mass of warm CGM of at least  $M_{CGM,warm} \gtrsim 10^{10} M_\odot$  to explain the observed O VI absorption (Peeples et al., 2014). This mass estimate is highly sensitive to the assumed metallicity in the warm CGM phase, and decreasing  $Z$  from  $Z_\odot$  to  $0.1Z_\odot$  increases the predicted warm CGM mass by a factor of 10. The constraints on the warm CGM fraction thus range from 0.6% to 6% of the total halo mass, or 4 – 40% of the expected baryon fraction.

X-ray observations hint at the existence of a hot ( $> 10^6$  K) gaseous reservoir outside large galaxies. Estimates of the total mass of this X-ray component range from  $10^9 - 10^{11} M_\odot$ . W14 argues that, by extrapolating the observed mass of  $\approx 10^9 M_\odot$ , observed within 50 kpc of an  $L^*$  galaxy by *ROSAT* (Anderson et al., 2013), to 300 kpc could increase the mass by a factor of 6 – 14, although the density profile of this X-ray component is unconstrained. W14 adopts the range of  $10^9 - 1.4 \times 10^{10} M_\odot$  for the X-ray CGM from this work. This is between  $\approx 1\%$  to  $5\%$  of the expected baryonic mass, or  $< 1\%$  of the total mass budget. Gupta et al. (2012), however, claims that the Milky Way may have a hot, X-ray reservoir with mass as high as  $10^{11} M_\odot$ , based on O VII and O VIII absorption observed with *XMM-Newton* and emission from the soft X-ray background. If this is true, the X-ray component of the CGM may be

substantially larger than observed by Anderson et al. (2013).

Allow us to summarize the distribution of the expected baryonic mass ( $M_b \approx 2.6 \times 10^{11} M_\odot$ ) in galaxy halos, as described above and by Werk et al. (2014). The gas in the cool CGM has at least 25% and as much as 50% of  $M_b$ . The stellar disk contains  $\approx 25\%$ , depending on the amount of gas in the ISM. The warm CGM contains between 4% and 40%, and the X-ray CGM is thought to hold 1%–5%. W14 concludes that current observations could be detecting the entire baryon fraction in galactic clusters, with the primary uncertainty resting on the contents of the warm CGM.

To fit a best estimate to the baryon fraction, we take the mean of the lower and upper limits on each component’s abundance, with the exception of the stellar-disk component, which we take to be the upper limit of 4.5% of the total halo mass from stars and ISM. We take one-half the range on the limits as the uncertainty:

$$\begin{aligned} f_{disk}(< r_{vir}) &= 0.045 \pm 0.013 \\ f_{CGM,cool}(< r_{vir}) &= 0.060 \pm 0.013 \\ f_{CGM,warm}(< r_{vir}) &= 0.035 \pm 0.025 \\ f_{X-ray}(< r_{vir}) &= 0.005 \pm 0.004 \end{aligned}$$

Summing these components and propagating uncertainties, assuming they are independent, yields our best estimate of the baryon fraction in galactic halos:

$$\mathbf{f_b}(< r_{vir}) = \mathbf{0.145 \pm 0.030} . \quad (2.17)$$

If the errors are not independent (and add linearly, not in quadrature), the true lower and upper limits on the baryon fraction in galactic halos are 9.5% and 19%, respectively.

# Chapter 3

## Results

### 3.1 The Distribution of Gas and Baryons in Groups and Clusters

From the observations presented in Chapter 2, we have measurements of the gaseous component of the ICM in halos spanning the entire mass range from poor groups to the most massive clusters. We also have measurements of the stellar fraction well beyond the virial radius, gathered from stacked optical and weak lensing observations. Here, we show our results from this data and its analysis.

In Figure 3.1, we present the gas fraction in these groups and clusters as a function of radius, out to  $1.2r_{vir}$ . We use the extrapolation methods described in Section 2.2.2 when necessary for observations which only constrain the gas fraction within  $r_{500}$  or  $r_{200}$ . The gas fractions of each sample (both observed and extrapolated) are listed in Table 3.1. We discuss the potential biases in using the hydrostatic mass and extrapolating the gas density profile to  $1.2r_{vir}$  in Section 4.1.

The gas fraction increases with radius in all groups and clusters. Comparing to the “expected” gas fraction of  $\approx 15.4\%$ , which is the difference between the WMAP9 cosmic baryon fraction (16.4%) and the cosmic stellar fraction of BK14 (1%), nearly

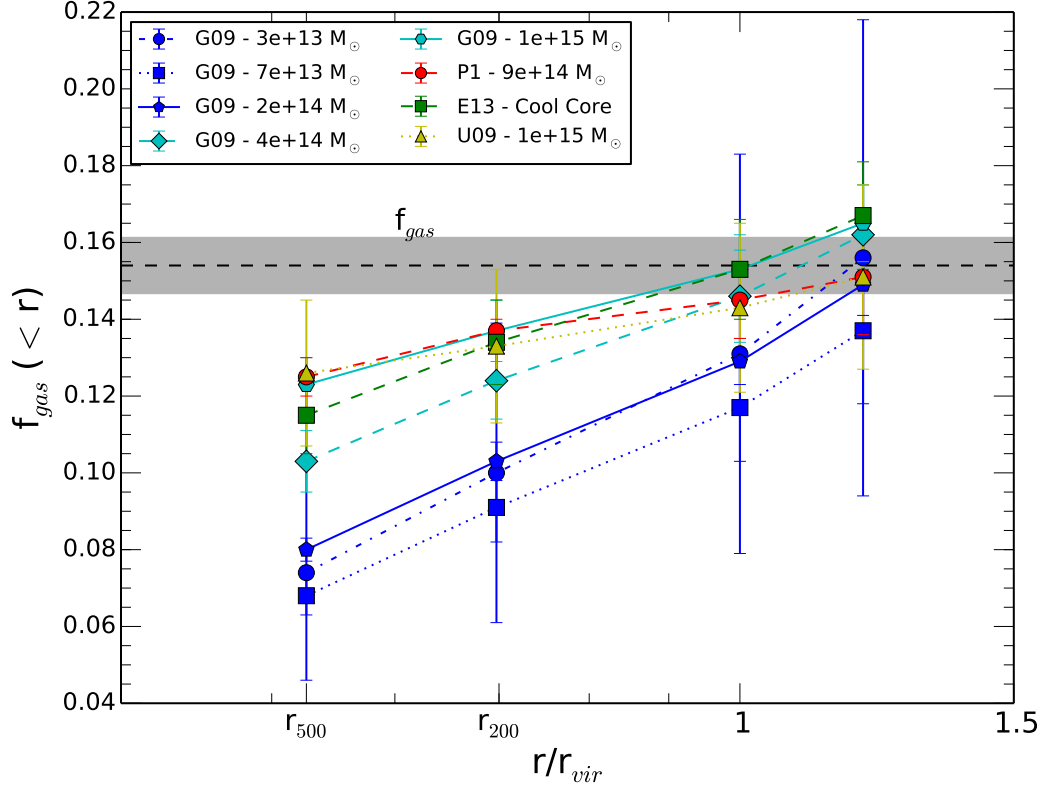


Figure 3.1: The cumulative hot gas fraction for each cluster sample in our study, plotted against the cluster-centric radius. Blue and cyan points (G09) represent data from Giodini et al. (2009), red points (P1) are temperature hypothesis 1 from Planck Collaboration (2013c), green points (E13) from Eckert et al. (2013c), and yellow points (U09) from Umetsu et al. (2009). See Section 2.2.1 for details of these sources. Many observations are extrapolated to  $1.2r_{vir}$ , as in Rasheed et al. (2011). The  $f_{gas}$  line represents the difference between the WMAP9 cosmic baryon fraction and the cosmic stellar fraction from Bahcall & Kulier (2014). We discuss possible biases in using the HSE mass and extrapolating the gas density profile in Section 4.1.

all clusters appear to contain the expected fraction of gas within the virial radius or  $1.2r_{vir}$ . A large portion of the ICM is, therefore, “hidden” in the outskirts of groups and clusters, where earlier observations interior to  $r_{500}$  were not able to probe.

Table 3.1: Gas Fraction in Groups/Clusters: Observed and Extrapolated

Reference (1)	$\langle kT \rangle$ (2)	$\alpha_{gas}$ (3)	$f_{gas,500}$ (4)	$f_{gas,200}$ (5)	$f_{gas,vir}$ (6)	$f_{gas,1.2vir}$ (7)
G09 Bin 1	0.9 keV	$1.7 \pm 0.20$	$0.074 \pm 0.028$	$0.100 \pm 0.039^*$	$0.131 \pm 0.052^*$	$0.156 \pm 0.062^*$
Bin 2	1.6 keV	$1.8 \pm 0.20$	$0.068 \pm 0.005$	$0.091 \pm 0.009^*$	$0.117 \pm 0.014^*$	$0.137 \pm 0.019^*$
Bin 3	2.8 keV	$1.9 \pm 0.07$	$0.080 \pm 0.003$	$0.103 \pm 0.005^*$	$0.129 \pm 0.006^*$	$0.149 \pm 0.008^*$
Bin 4	5.0 keV	$2.1 \pm 0.02$	$0.103 \pm 0.008$	$0.124 \pm 0.010^*$	$0.146 \pm 0.012^*$	$0.162 \pm 0.013^*$
Bin 5	8.6 keV	$2.3 \pm 0.02$	$0.123 \pm 0.007$	$0.137 \pm 0.008^*$	$0.153 \pm 0.009^*$	$0.165 \pm 0.010^*$
PC13	†	†	$0.125 \pm 0.005$	$0.137 \pm 0.003$	$0.145 \pm 0.010$	$0.151 \pm 0.009$
E13 - CC	6.3 keV	$2.2 \pm 0.05$	$0.115 \pm 0.010$	$0.134 \pm 0.011$	$0.153 \pm 0.013^*$	$0.167 \pm 0.014^*$
U09	9.7 keV	$2.4 \pm 0.10$	$0.126 \pm 0.019$	$0.133 \pm 0.020$	$0.143 \pm 0.022^*$	$0.151 \pm 0.024^*$

(1) Reference abbreviations as in Table 2.1.

(2) The median temperature of the groups/clusters in each sample.

(3) The gas density slope derived from R11.

(4)  $f_{gas}(< r_{500})$  (5)  $f_{gas}(< r_{200})$  (6)  $f_{gas}(< r_{vir})$  (7)  $f_{gas}(< 1.2r_{vir})$

\*: Value represents extrapolation using the method of Section 2.2.2.

†: No extrapolation required; T and  $\alpha_{gas}$  not calculated.

Figure 3.2 shows the halo gas fraction as a function of the virial mass of the halo. The shortage of gas in low-mass clusters is apparent at  $r_{500}$ , with low-mass groups and clusters falling further short of the expected fraction than larger clusters. However, the shallower slope of the gas density profile in low-mass halos leads to a dramatic increase in the gas fraction when extrapolated to higher radius: from  $r_{500}$  to  $r_{vir}$ , their gas fraction has almost doubled. The gas distribution in low mass clusters is more extended, likely due to the shallow gravitational potential well. This is also consistent with the stellar mass distributions of BK14, indicating that the stellar fraction is more extended in groups and poor clusters. All halos are consistent with containing the expected gas fraction interior to  $\approx 1.2r_{vir}$ . Gas is less centrally concentrated than dark matter, with a large fraction residing in the outskirts of groups and clusters, but within  $1.2r_{vir}$  the gas mass traces the total mass well.

The mass of dark matter halos clearly has an important effect on the distribution

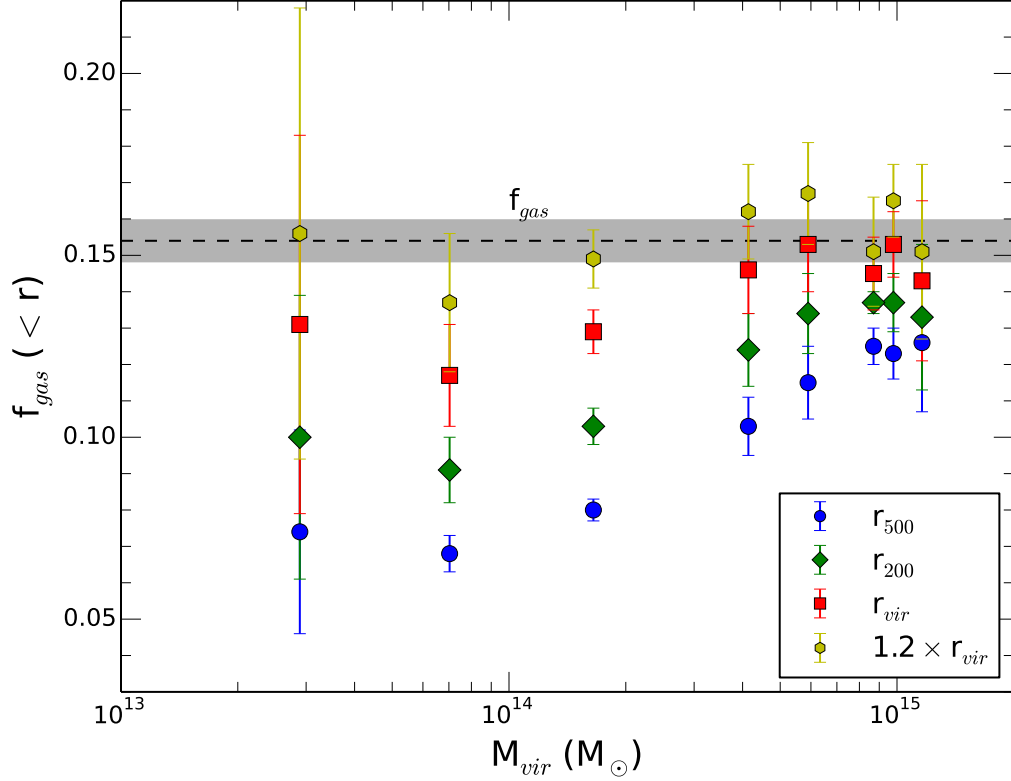


Figure 3.2: The cumulative hot gas fraction for each cluster sample in our study, plotted against the mean halo mass. Blue circles, green diamonds, red squares, and yellow hexagons show the gas fraction measured at  $r_{500}$ ,  $r_{200}$ ,  $r_{vir}$ , and  $1.2r_{vir}$ , respectively. The  $f_{gas}$  line represents roughly the expected hot-gas fraction, and is the difference between the *WMAP9* cosmic baryon fraction and the cosmic stellar fraction ( $\approx 1\%$ , Bahcall & Kulier, 2014).

of baryons, as the halo mass appears to determine how extended the baryonic distribution is. We therefore combine our samples of groups and clusters into two bins: groups/poor clusters ( $M_{vir} < 3 \times 10^{14} M_{\odot}$ ), and rich clusters ( $M_{vir} > 3 \times 10^{14} M_{\odot}$ ). In Figure 3.3, we show the averaged gas fraction in each bin, as a function of radius. Each point represents the weighted mean of gas fraction at that radius, for all clusters in that mass range. These mass bins translate roughly to the medium-richness and high-richness bins of BK14, respectively. Therefore, we also include the average stellar fraction, which is measured far beyond  $r_{vir}$ .

At  $r_{500}$ , the average gas fraction is  $\approx 7.5\%$  in groups and poor clusters and  $\approx$

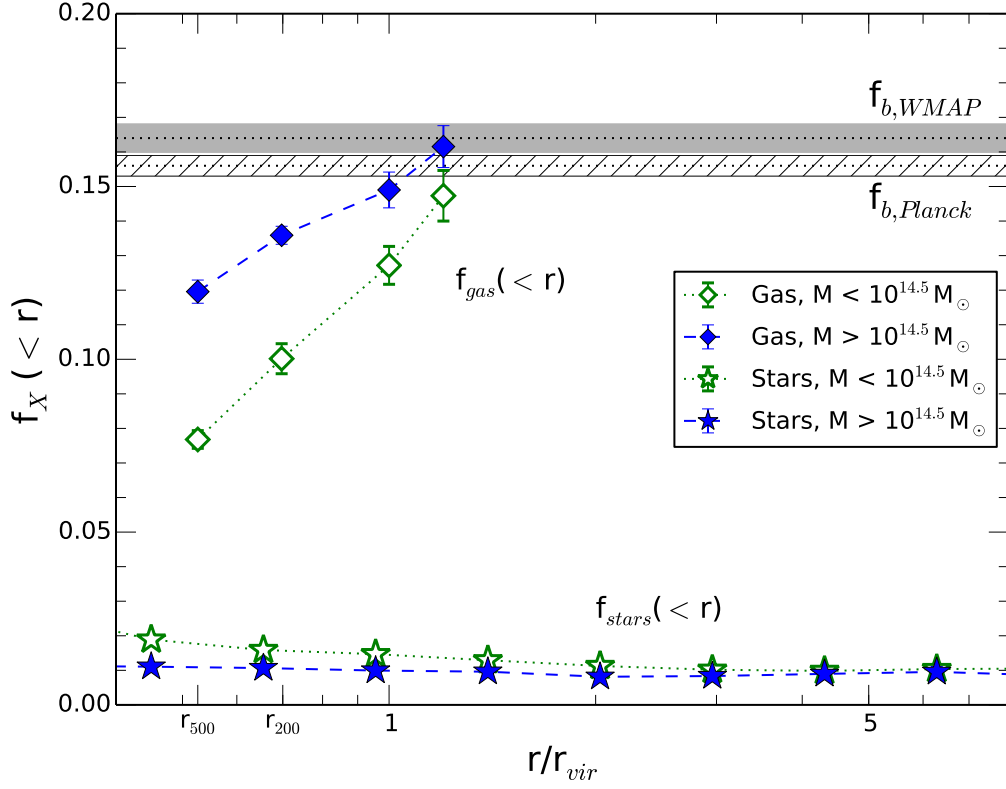


Figure 3.3: The cumulative stellar (Figure 2.2) and hot gas (Figure 3.1) fractions for groups and clusters, as a function of cluster-centric radius. Bahcall & Kulier (2014) presented the stellar fraction for various cluster richness bins. The gas fractions of Figure 3.1 have been sorted into corresponding bins, using the mass-richness relation of Sheldon et al. (2009b). The stellar fraction asymptotes to a “cosmic” stellar fraction at a few times  $r_{vir}$ , and the gas fraction increases and converges at high radius as well.

12% in rich clusters. The gas fraction increases steeply in groups and poor clusters, reaching about 13% at  $r_{vir}$  and 15% at  $1.2r_{vir}$ . In rich clusters, the gas fraction increases more slowly, reaching 15% at  $r_{vir}$ , and 16% at  $1.2r_{vir}$ , representing the increased concentration of gas in high mass clusters. The stellar fraction decreases from 2% at  $r_{500}$  to 1.5% at  $1.2r_{vir}$  in the low-mass bin, and remains steady at 1% in the high-mass bin. We note that the apparent steepening of the  $f_{gas}$  profile at  $r_{vir}$  is simply a relic of the logarithmic scale of the X axis. As a whole, low mass clusters have lower gas fractions and higher stellar fractions at any given radius, with both distributions being more extended than in massive clusters.



We are now able to combine the gas fraction and stellar fraction for clusters in these two mass ranges, yielding the total baryon fraction distribution. This is presented in Figure 3.4. The overall baryon fraction increases with radius, reaching the cosmic baryon fraction at  $\approx r_{vir}$  in massive clusters and at  $\approx 1.2r_{vir}$  in groups and poor clusters. The entire baryonic mass associated with the halo mass of groups and clusters is detected or inferred within the dark matter halo, indicating that the baryonic matter content of the universe is a strong proxy for the dark matter distribution, when averaged on appreciably large scales.

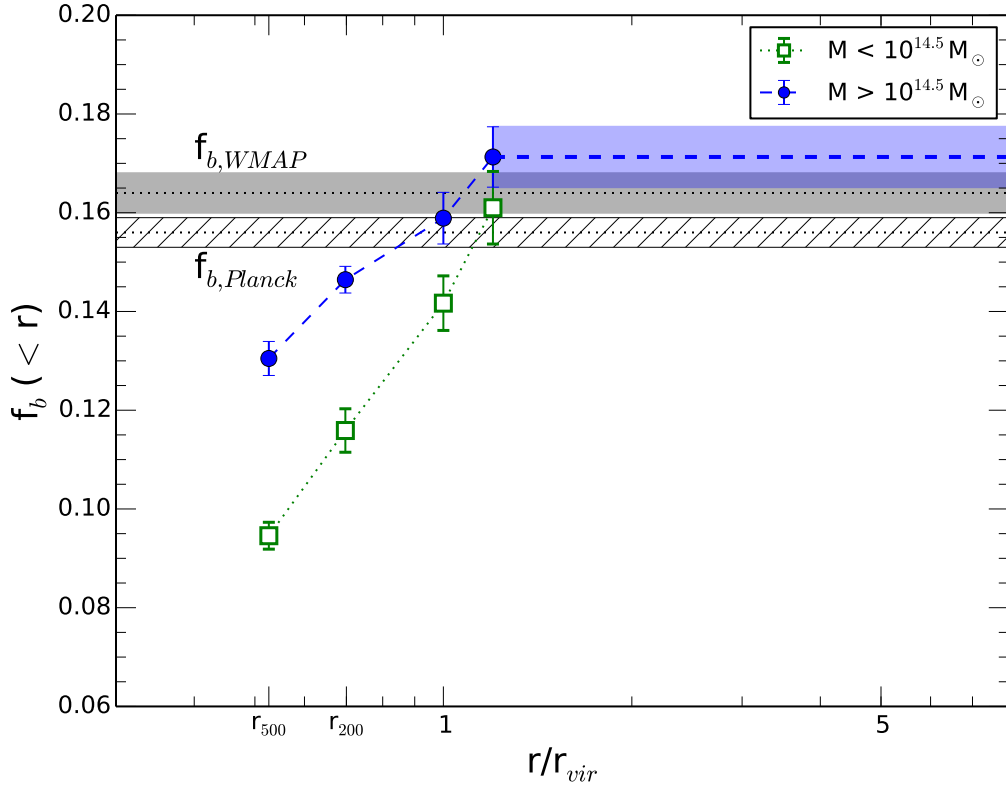


Figure 3.4: The cumulative baryon fraction for groups and clusters, as a function of cluster-centric radius. The baryon fraction ( $f_b$ ) is the sum of the cumulative stellar fraction and the cumulative hot gas fraction of Figure 3.3. Green squares represent the averaged fractions of groups and smaller clusters, while blue circles represent larger clusters. The baryon fraction in large clusters appears to approach the cosmic fraction at large scales, and we extrapolate the value at larger scales as the value at  $1.2r_{vir}$ , an assumption we discuss in Section 4.1.3.

The stellar fraction is observed to approach a constant value at high radii (Bahcall & Kulier, 2014). The gas fraction is predicted to do the same, as the gas density profile likely approaches the total mass (NFW) profile at high radius (e.g., Umetsu et al., 2009, and refs. therein). We approximate this by assuming that, beyond  $\approx 1.2r_{vir}$ , the gas fraction reaches a constant value, and represent this as an extrapolation of the baryon fraction out to high radius in Figure 3.4. Therefore, current observations are consistent with the picture that the baryon distribution matches the distribution of matter well at all scales larger than the virial radius of clusters. The extrapolation to  $1.2r_{vir}$  and not beyond is arbitrary, as the gas density slope likely steepens before this point. We discuss this simplification and the validity of our approximation in Section 4.1.3.

## 3.2 The Baryonic Content of Dark Matter Halos

We have just shown that, within roughly the virial radius, dark matter halos of both group and cluster sizes are observed to hold the entire cosmic baryon fraction. Combined with the measurements of the baryonic components in galactic halos (Section 2.4.2), we are able to place global constraints on the baryon distribution within halos ranging over three orders of magnitude in mass.

Figure 3.5 presents the collection of observations on the baryon fraction in halos of a wide range of masses. Shown, as a function of mass, are the current limits on the baryon fraction for the previously mentioned samples of galaxies, groups, and clusters. Observations of the outskirts of groups and clusters show that the baryon fraction reaches the cosmic value between  $r_{vir}$  and  $1.2r_{vir}$ . We plot the group and cluster baryon fraction, which is the sum of the gas fraction (Figure 3.2) and stellar fraction (Figure 2.2) for halos, at these two radii and sorted by mass. Observations of galactic halos show that – between the stellar disk and ISM, cold CGM, warm CGM, and

X-ray CGM – the entire baryon fraction could be contained within the virial volume of galaxy halos. We plot the baryon fraction range constrained by Werk et al. (2014), which includes lower and upper limits of  $f_b(< r_{vir}) = 9\% - 19\%$ . The best-estimate value, taking the mean of the ranges given for each component, is  $14.5\% \pm 3\%$ .

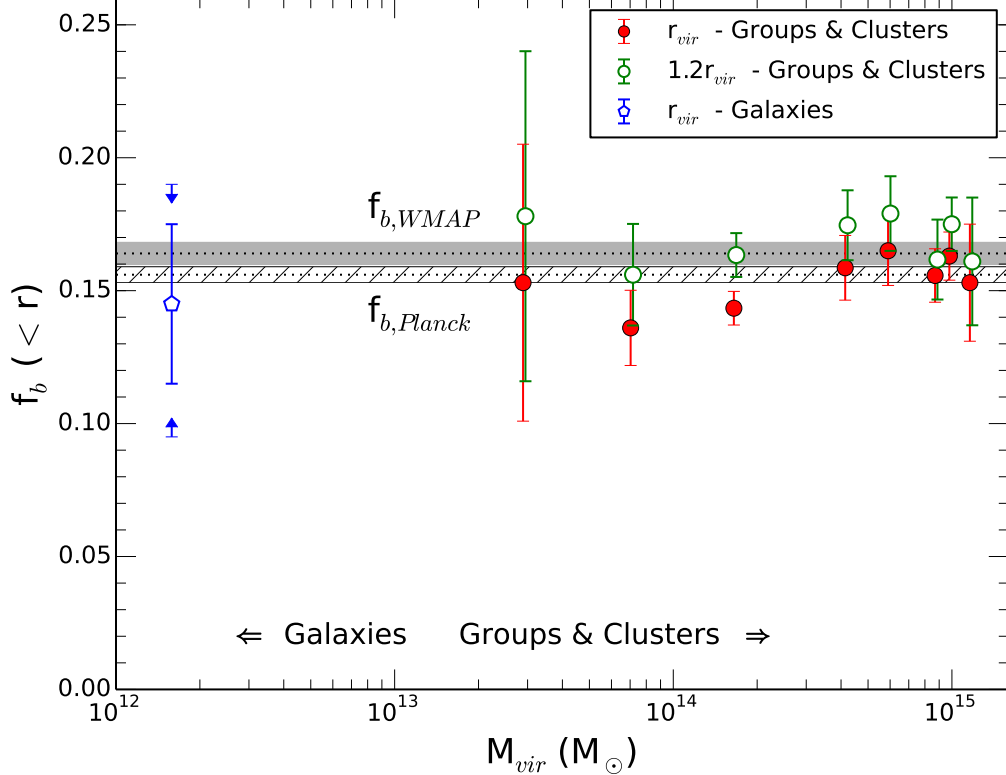


Figure 3.5: The cumulative baryon fraction ( $f_b$ ) for galaxies, groups, and clusters, as a function of the average mass of the sample. The baryon fraction of groups and clusters (filled red points: within  $r_{vir}$ ; open green points: within  $1.2r_{vir}$ ) is the sum of the cumulative stellar and hot gas fractions of Figures 2.2 and 3.2. The baryon fraction of  $L^*$  galaxies (open blue point) is gathered from Werk et al. (2014). The arrows indicate upper and lower-limits on the galaxy baryon fraction, while the error-bars represent the propagated error on the fraction, assuming independent uncertainties on the different galactic components (Section 2.4.2).

Groups and poor clusters are still slightly short of baryons within the virial radius (shown by red points in Figure 3.5). However, there is no reason to assume that the gas density must cut-off suddenly at this relatively-arbitrary point. Direct

observations (Planck Collaboration, 2013d) indicate that the gas fraction in massive clusters continues to increase beyond  $r_{vir}$ . Hence groups and poor clusters (where the baryon distribution is observed to be more extended than in massive clusters) should also have large baryon reservoirs beyond this radius, which justifies our choice to extrapolate  $f_{gas}$  to  $1.2r_{vir}$ .

From galaxies to the most massive clusters, current observations are consistent with the entire baryon fraction being contained within the dark matter halo. Integrating out to  $r_{vir}$  and slightly beyond, there is no significant shortage of baryons, even in low-mass clusters and galactic halos, where previous estimates claimed a dramatic lack of baryonic mass. Considering the entire range of mass, there does not appear to be any strong correlation between enclosed baryon fraction with mass. The baryonic mass traces accurately the dark matter mass in halos, and there should not be any excess of baryons in voids or the IGM. Therefore, in response to the question “Where are the baryons in the universe”, we show that baryons have fallen into and stayed within dark matter halos, and trace closely the total mass distribution in the universe.

# Chapter 4

## Discussion

### 4.1 Limitations and Observational Biases

Due to the extreme sensitivity required to accurately measure the gas mass and total mass in clusters, our methods have included several assumptions (such as that the ICM is in hydrostatic equilibrium, and that the gas density slope is constant beyond  $r_{500}$ ) which require additional discussion. Here, we discuss theoretical and observational constraints on the magnitude of possible biases which we introduce by making these simplifications.

#### 4.1.1 Assumption of Hydrostatic Equilibrium in Calculating Total Mass

As was highlighted throughout Chapter 2, there are several different ways to calculate the total mass of group and cluster halos. One key characteristic of a mass estimation method is whether it relies on the assumption of hydrostatic equilibrium. The so-called “hydrostatic mass” ( $M_{HSE}$ ) can be calculated by combining the gas density profile with either the temperature or pressure profile, a method ubiquitous in X-ray observations. Using mass-scaling relations (such as the  $Y_{SZ}$ - $M_{500}$  relation) may also

be sensitive to the assumption of HSE if the relation is calibrated against hydrostatic masses. Masses which do not rely on the assumption of HSE are primarily derived from gravitational lensing.

Hydrostatic masses could be systematically biased, relative to the “true” mass (usually assumed to be the lensing mass,  $M_{WL}$ ) if there are significant sources of non-thermal pressure in the ICM. Examples include kinetic bulk motions or magnetic fields. Hydrostatic equilibrium assumes that the gravitational force (the total mass) is offset by the pressure gradient, so assuming that only the gas pressure contributes can lead to a bias in the inferred mass.

The magnitude of the hydrostatic mass bias is of paramount importance to precision cosmology. Cosmological parameters (such as  $\Omega_m$ ) derived from *Planck* cluster counts and hydrostatic mass estimates disagree significantly from values derived directly from the CMB power spectrum, but a large hydrostatic mass bias ( $b = 1 - M_{HSE}/M_{WL} \approx 0.3$ ) could relieve the observational tension (Gruen et al., 2013; von der Linden et al., 2014; Israel et al., 2014). Such a large bias on the total halo mass would also dramatically affect the gas fraction derived using hydrostatic masses, affecting its use as a cosmological probe (e.g., Grego et al., 2001; Ettori et al., 2009). As the majority of our  $f_{gas}$  measurements in clusters were measured relative to hydrostatic masses (with the exception of Umetsu et al. (2009)), our results are likewise sensitive to the hydrostatic bias.

Cosmological simulations are a major tool used to constrain this bias. The mass of simulated clusters can be compared to mock X-ray observations which assume hydrostatic equilibrium, determining the bias factor as a function of mass and overdensity. Simulations nearly unanimously indicate that the hydrostatic mass is biased low compared to the true halo mass ( $b > 0$ ), a bias which increases towards the outskirts of clusters or in unrelaxed clusters, where merger disruptions and bulk flows become more significant. Different simulations and physical prescriptions place the bias any-

where from 5% (e.g., Lau et al., 2009; Meneghetti et al., 2010; Burns et al., 2010; Nelson et al., 2012) to 20% (e.g., Arnaud et al., 2007; Nagai et al., 2007; Battaglia et al., 2013).

Observational constraints on the hydrostatic mass bias vary widely, however. Some weak lensing measurements of clusters suggest that hydrostatic X-ray or SZ masses are biased low by 10% (Andersson et al., 2011; High et al., 2012), and others indicate this bias could be as large as 20 – 30% (Arnaud et al., 2007; Ichikawa et al., 2013; von der Linden et al., 2014). Yet others find no significant difference between weak lensing masses and hydrostatic masses, with some hints that hydrostatic equilibrium assumptions may even *overestimate* the true mass in lower-mass clusters (Gruen et al., 2013; Israel et al., 2014). Figure 4.1, from Gruen et al. (2013), shows the agreement in their measured weak lensing and hydrostatic masses.

The issue of hydrostatic mass bias is far from solved. Due to the inconsistent observational and simulated constraints, it is unclear how large of a hydrostatic correction factor should be included in our measurements of the gas fraction, or if one is even necessary. A bias low in the hydrostatic mass would bias the gas fraction high, meaning that groups and clusters are slightly more deficient of baryons than we suggest. Our choice to avoid using a hydrostatic correction factor until this issue is clarified is slightly justified by the fact that one of our samples (U09) measures gas fraction against the weak lensing mass, and this fraction agrees well with gas fraction derived from the HSE assumption.

#### 4.1.2 Gas Clumping in Cluster Outskirts

The primary means of deriving the gas density profile of clusters is from measurements of X-ray surface-brightness, which scales with the square of electron density. Due to this  $n^2$  dependence, clumpy and overdense structures in the ICM will emit more than their share of X-ray luminosity, biasing gas density measurements high. The

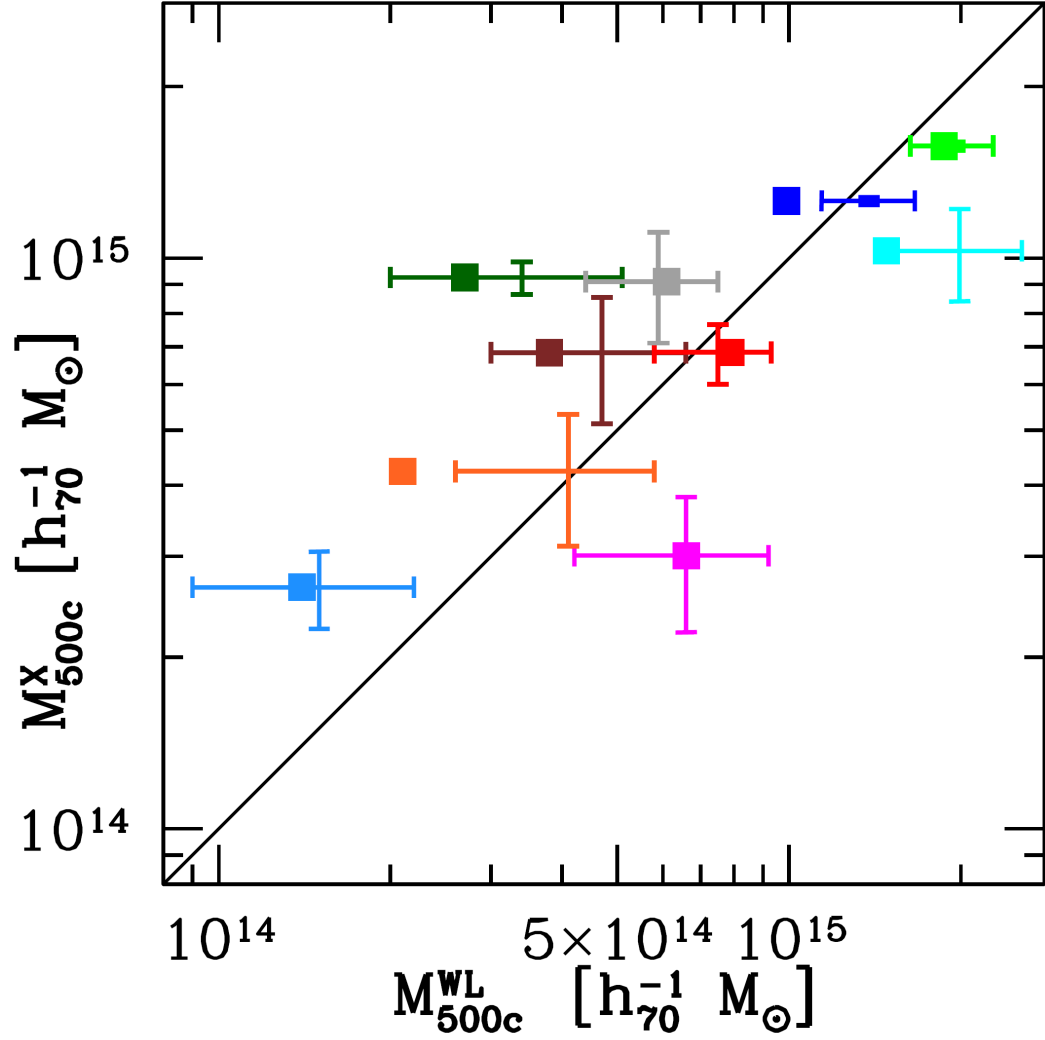


Figure 4.1: A comparison of weak lensing masses ( $M_{500c}^{WL}$ ) and X-ray hydrostatic masses ( $M_{500c}^X$ ) for SZ clusters, as presented in Gruen et al. (2013). Error bars indicate the best-fit “single-halo” fit, while the filled symbols include corrections to  $M^{WL}$  for other structures in the field of view. In tension with simulations, the authors find that hydrostatic masses are not systematically biased low relative to the weak lensing mass.



magnitude of this bias depends on the smoothness of the ICM gas distribution, which can vary widely from cluster to cluster.

Simulations typically predict a clumping bias (overestimate of  $M_{gas}$ ) of  $\approx 10 - 15\%$  (Nagai & Lau, 2011; Battaglia et al., 2013), which increases in unrelaxed clusters and towards cluster outskirts, where recent interactions have a more significant dynamical effect. This could explain the large differences in measured gas fraction between CC and NCC clusters, although observations suggest that the level of clumpiness is overestimated in simulations, and that the average bias is below 10% (Eckert et al., 2013b). The majority of our cluster samples represent relaxed (CC) clusters, so we do not include a clumping bias factor in our analysis. We also note that the P13 (Planck Collaboration, 2013d) and U09 (Umetsu et al., 2009) gas fractions are derived from SZ measurements, which do not suffer from this clumping bias, and agree well with our X-ray data sets.

### 4.1.3 Extrapolation of the Density Profile Slope

The choice to extrapolate the gas fraction to  $1.2r_{vir}$  and then stop is arbitrary. Between  $r_{500}$  (where  $\alpha_{gas}$  is well measured) and  $r_{200}$ , observations disagree whether the slope remains roughly constant (Dai et al., 2010) or steepens by roughly 10% (Ettori & Balestra, 2009). Assuming the true evolution is somewhere in between, the gas density slope should not change appreciably relative to the total mass (NFW) profile, which steepens by about 4% within this range. Therefore, our simplified model that  $\alpha_m$  and  $\alpha_{gas}$  remain constant beyond  $r_{200}$  should roughly approximate the increase of  $f_{gas}$  with radius.

It is expected that the slope will eventually asymptote to match the total mass (NFW) profile (Umetsu et al., 2009; Battaglia et al., 2013), suggesting that, at large radius,  $\alpha_{gas}$  will steepen more quickly than  $\alpha_m$ . The point at which this occurs is not well constrained, but it will taper the growth of  $f_{gas}$ , which should eventually reach

a constant value, similar to the stellar fraction. Planck Collaboration (2013d) finds that the gas fraction in stacked *Planck* clusters flattens out between 1 and  $1.5r_{vir}$ . We approximate this by extrapolating  $f_{gas}$  as constant above  $1.2r_{vir}$ . However, until temperature measurements beyond  $r_{500}$  improve, the true radius where the baryon fraction reaches a maximum will remain unconstrained.

## 4.2 Comparison to Simulations

As discussed above, cosmological simulations have frequently been used to examine the magnitude of observational biases on measurements of cluster properties. Here we discuss the simulated cluster properties themselves, from the simulations of **Battaglia et al. (2013)**. We have discussed above that these simulations suggest that the assumption of HSE may bias our observed gas and baryon fractions low. Here, we neglect these biases and compare the trends in their simulated gas and baryon fraction to our observations, having concluded earlier that the issue of mass bias is not yet settled.

The authors conducted a series of smoothed particle hydrodynamic (SPH) simulations with three different physical feedback prescriptions: 1) a “shock-heating” only method, 2) a method that also included radiative cooling and star formation/supernovae feedback, and 3) a prescription including AGN thermal feedback. The simulations produced (at  $z = 0$ ) a sample of over 1000 clusters with  $M_{200} > 7 \times 10^{13} M_{\odot}$ , and 800 above  $10^{14} M_{\odot}$ .

Figure 4.2 shows the cumulative stellar, gas, and baryon fractions in the simulated clusters, as a function of mass (compare to our Figure 3.2). In the shock heating and radiative cooling models, the total baryon fraction within  $r_{200}$  is nearly the cosmic value in all clusters ranging from  $10^{14} - 10^{15} M_{\odot}$ . In the AGN feedback model,  $f_b$  decreases in smaller halos, due primarily to suppressed stellar mass production,

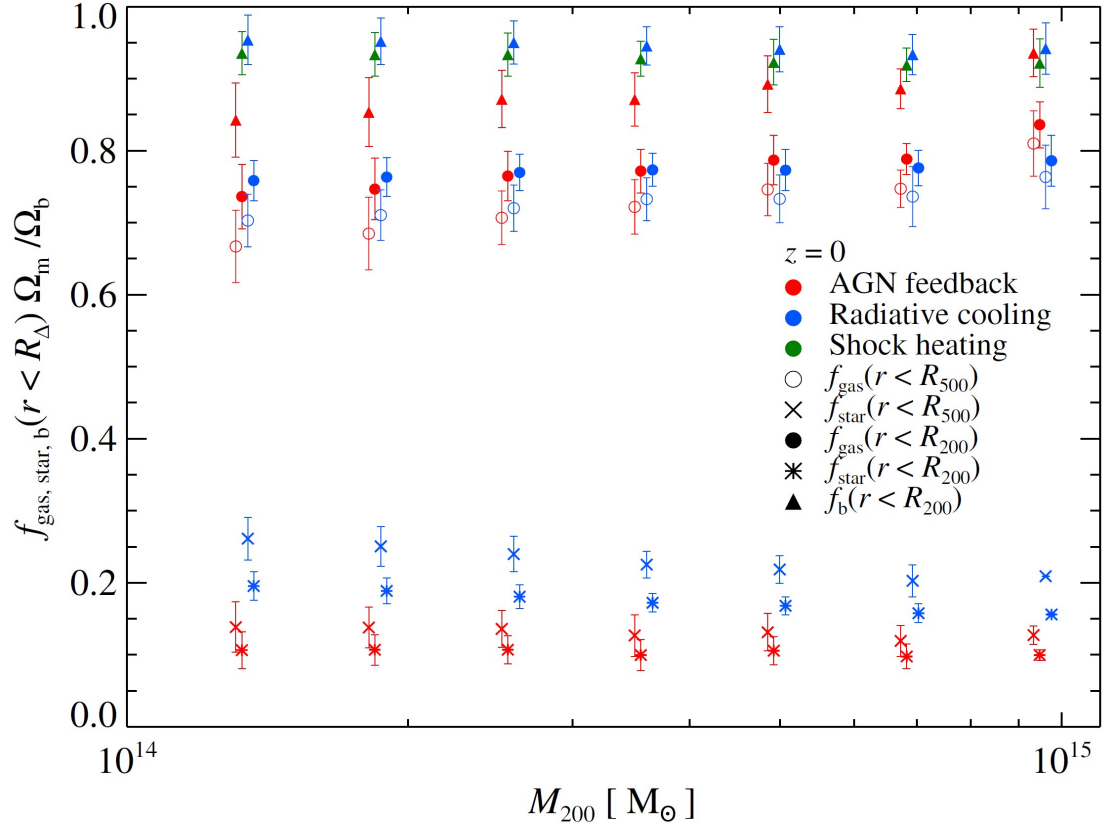


Figure 4.2: The gas, stellar, and baryon fraction (scaled by the cosmic baryon fraction) as a function of cluster mass from a series of simulations by Battaglia et al. (2013). The baryon fraction within  $r_{200}$  is close to the cosmic value for the entire mass range of  $10^{14} - 10^{15} M_{\odot}$ , except for in the AGN feedback model, where low-mass clusters have fewer baryons within  $r_{200}$ . These simulations are in agreement with our results, although the simulations predict a large hydrostatic mass bias (Section 4.1.1) that has yet to be confirmed observationally.

although partly due to increased non-thermal pressure pushing the gas towards higher radius. These simulations are in agreement with our results that conclude the entire baryon fraction can be recovered in clusters of all mass ranges.

Figure 4.3 presents the radial distribution of the gas, stellar, and baryon fractions for clusters binned by mass. Only the results for the AGN feedback model are presented. The stellar fraction decreases significantly from the center of the clusters, with a higher stellar fraction in low-mass clusters for any given radius. In all mass bins, however, the stellar fraction asymptotically approaches a “cosmic” value of  $\approx 10\%$

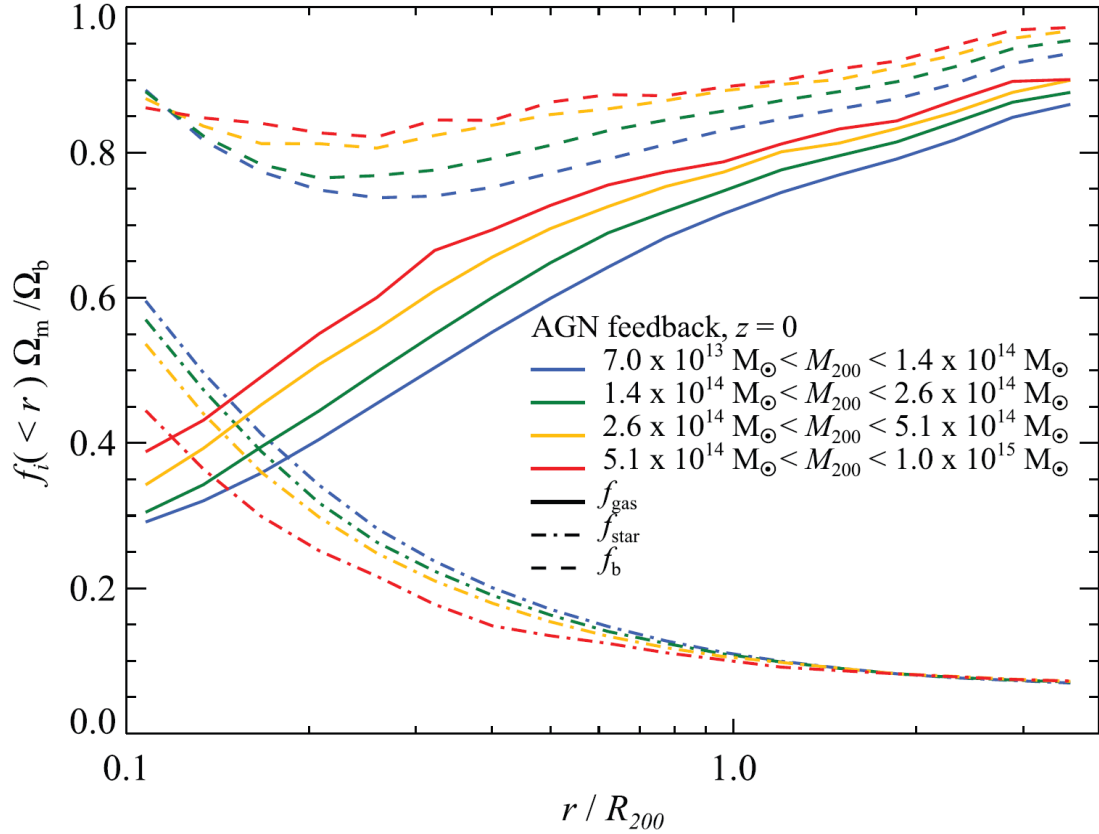


Figure 4.3: The gas, stellar, and baryon fraction distributions (scaled by the cosmic baryon fraction) as a function of radius in the simulations of Battaglia et al. (2013), binned in four parts by cluster mass. The stellar fraction and gas profiles match observations well, and the total baryon fraction approaches the cosmic value at high radius.

of the baryon fraction. This behavior matches very well the stellar fraction profile measured by Bahcall & Kulier (2014), although the asymptotic fraction (relative to the baryon fraction) is higher than observed ( $\approx 6\%$ ).

The gas fraction profile also matches our observed trends well. The gas fraction in the central regions of low mass clusters is significantly lower but increases more rapidly with radius than in high-mass clusters. The gas fraction in clusters of all mass converges towards the same profile at high radius. Of particular interest, however, is that even at  $r > 3r_{200}$  the gas fraction is still increasing steadily. If this represents the gas profile in real clusters (different feedback models have different behavior in

the outskirts), then the our assumption that the gas fraction remains constant above  $1.2r_{vir}$  may need adjustment.

The overall baryon fraction increases from a minimum of  $70 - 80\%$  cosmic around  $0.5r_{200}$  to  $> 90\%$  outside the virial radius. The fact that the baryon fraction does not reach the cosmic fraction until very high radius ( $> 4r_{200}$ ) is in slight tension with our results, and improved observations of the gas profile slope beyond  $r_{200}$  will help constrain whether these simulations accurately predict how far beyond the virial radius the baryons are extended. Additionally, the simulations assume a cosmic baryon fraction of  $f_b = 0.172$ , higher than current observational estimates. The increased baryon abundance could lead to enhanced feedback effects, pushing baryons further from the cluster centers than actually observed. Simulations which match the current cosmological constraints would help clarify this issue.

Finally, in Figure 4.4, we show the redshift evolution in the gas fraction of the Battaglia et al. (2013) simulated clusters. Measured from the cluster centers to far beyond the virial radius, the gas fraction appears constant with redshift at all radii, with the exception of a slight decrease within  $2r_{200}$ . Measured from  $z = 1.5 - 0$ , this shows remarkable stability within the ICM over many gigayears, including the phase when the most massive clusters begin to form.

## 4.3 Implications

Having addressed the possible observational biases in our measurements and comparing our results to simulations, we address the global conclusions about the distribution of baryons that our results allow us to make. Understanding how baryons are distributed relative to dark matter and what relative forms they take in different halos will constrain how accurately baryons can be used as cosmological tools.

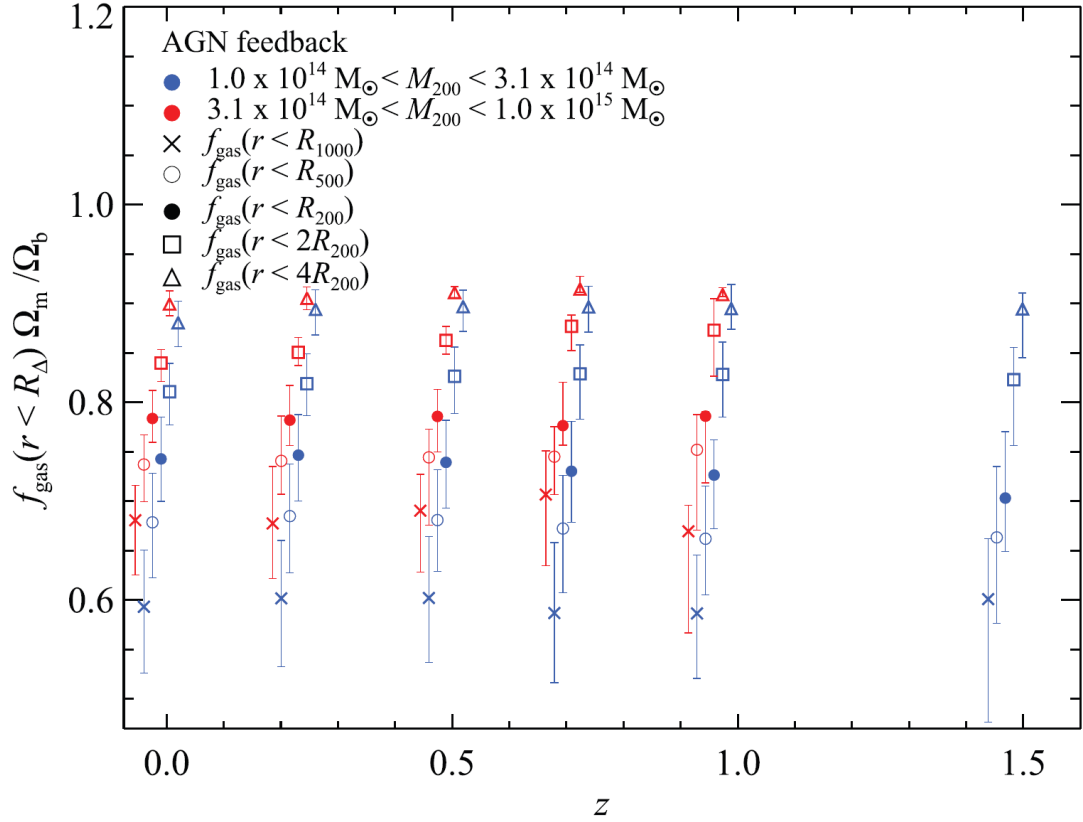


Figure 4.4: The gas fraction (scaled by the cosmic baryon fraction) within various radii, as a function of redshift, as measured by the simulations of Battaglia et al. (2013), and binned by mass. There is no significant redshift evolution of the gas fraction within any given radius, except possibly within  $2r_{200}$ , suggesting that measurements of the cluster baryon fraction should be fairly redshift independent back to  $z \approx 1$ , where massive clusters first begin to form.

#### 4.3.1 Deviations from Self-Similarity

Dark matter halos (both observationally and in simulations) are found to fit the NFW density profile, and hence are, roughly, “self-similar”. This means that all dark matter halos have the same proportions and shapes, varying only by overall size. Assuming only gravitational collapse, physical properties of baryons in clusters (such as pressure and temperature) would be expected to obey “universal profiles”, once scaled to the appropriate halo size (e.g., Arnaud et al., 2010; Planck Collaboration, 2013d).

Although we have shown that the entire baryonic mass can be accounted for in

halos ranging over three orders of magnitude in mass, the concentrations of gas and stellar fractions vary with halo mass. Pure self-similarity would suggest that the baryon fraction should reach the cosmic value at the same overdensity (such as  $r_{200}$  or  $r_{100}$ ) regardless of halo mass. However, observations of the gas fraction (Section 3.1) and the stellar fraction (Bahcall & Kulier, 2014) in clusters indicate that the scale at which these fractions asymptote to the cosmic values decreases with cluster mass. Baryons in less massive halos are extended farther relative to their virial radii than in massive clusters, an observation which is supported by cosmological simulations (Battaglia et al., 2013).

Therefore, baryonic physics plays an important role in shaping the distribution of baryons on scales smaller than the virial radius in halos. Feedback effects (such as merger shocks, AGN feedback, and star formation) are able to push baryons further into the outskirts of small halos than in large halos, due to the decreased gravitational potential. However, as our results indicate, these feedback effects are not so powerful as to remove a substantial fraction of baryons from the halos altogether, and nearly the entire baryon fraction remains bound to dark matter halos.

### 4.3.2 The Contribution of Individual Galaxies to Clusters

Bahcall & Kulier (2014) found that the overall mass-to-light ratio of clusters matches closely the average mass-to-light ratio of individual galaxies, when normalized by the changing ratio of elliptical and spiral galaxies with cluster radius (the “density-morphology relation”). This is consistent with the picture that the entire dark matter content of clusters is comprised of the dark matter originally bound to galaxy halos, which fell into the clusters and was stripped to form the cluster halo. There is no reason, they argue, to assume that groups and clusters contain more dark matter (relative to light) than individual galaxy halos do (unlike as predicted by e.g., Ostriker et al., 1974; Guo et al., 2010).

Our results suggest a similar interpretation involving the entire baryonic content of clusters. We show that clusters of all sizes contain the cosmic fraction of baryons within about the virial radius, distributed in about 15 parts hot ICM gas to 1 part stellar mass. Yet, combining the stellar mass of galaxies with observations of the multiphase CGM gas, Werk et al. (2014) demonstrated that large,  $L^*$  galaxies also contain approximately the cosmic fraction of baryons within their halos. If clusters form entirely from the disruption of infalling galaxies, then the galaxies would bring a baryon abundance equal to the cosmic fraction with them, filling clusters with dark matter, stars, and gas from their halos. Clusters do not necessarily need a separate source of non-galactic baryons to explain the high abundance of baryons in their halos: the cluster baryons could be comprised entirely of the baryonic mass once held in the halo of constituent galaxies. The ICM, therefore, could be the stripped remains of galactic ISMs and CGMs, with the stellar disks either remaining as cluster galaxies or being dispersed as the diffuse intracluster light (ICL).

One inconsistency that arises in this model is the stellar makeup of the baryons in halos: around 15% of the baryons in  $z = 0$   $L^*$  galaxies in the field are held in stars, while the stellar mass of clusters is only  $\approx 6\%$  of their baryons. As stars themselves are not destroyed when galaxies fall into clusters, one possible explanation for this discrepancy is a quenching of any further star formation in the galaxies that fall into clusters. Due to the hot, relatively dense ICM, collisional heating of the ISM of infalling galaxies could prevent these galaxies from forming stars. The stellar fraction in clusters could be explained if galaxies which merged into clusters had  $\approx 2.5$  times lower stellar mass than presently observed field galaxies, leaving the remainder of the baryons in a gaseous phase to populate the ICM. This level of star formation suppression is high, but not unreasonable. Most large clusters collapsed around redshift  $z = 1 - 1.5$  (Eke et al., 1996; Battaglia et al., 2013) and while the galactic star formation rate (per year) peaked around  $z = 2 - 3$ , a large majority of



stellar mass formed during the long period between  $z = 2 - 0$  (Hopkins & Beacom, 2006). Even if star formation suppression of this magnitude did not occur, we can place a lower limit on the total contribution by galaxies to the baryons (and dark matter) of clusters using the observed ratio of stellar fraction.

In the conservative case, let us assume that the entire stellar mass of galaxies formed during the peak of star formation, such that galaxies are not forming any stars during the period of cluster growth, and that there is no inherent difference between galaxies which will fall into clusters and those that will not. Therefore, the current observed stellar fractions of field galaxies (15%) represents accurately the stellar fraction of cluster galaxies just before they merge. Assuming no stars are formed except in galaxies, then the total stellar fraction in clusters (6%) came entirely from the previously formed stars of merging galaxies. Galaxies, therefore, must have contributed  $6/15 = 40\%$  of the total mass of clusters, with the remaining 60% coming from diffuse IGM gas which collapsed into the cluster along with the galaxies.

This estimate represents a lower limit, due to the assumption of no star formation past  $z \approx 2$ . In reality, stellar mass buildup has continued strongly to  $z = 0$ , such that galaxies which began merging into clusters at  $z \approx 1$  likely had a stellar fraction lower than 15%. In this case, star formation in cluster galaxies was likely quenched when falling into clusters, lowering the stellar mass of each constituent galaxy, and raising our estimate of the galactic contribution to clusters.

According to the models of Hopkins & Beacom (2006), the accumulated stellar mass in galaxies at  $z = 1$  was only  $\approx 60\%$  its current value, and only 45% at  $z = 1.5$ . If galaxies had a 50% overall quenching in star formation after falling into clusters at  $z = 1.5$ , their current stellar fraction would be 11%, suggesting that individual galaxies contributed  $> 50\%$  of the matter of clusters. An 80% suppression of star formation would raise the galactic contribution to clusters to 70%.

### 4.3.3 Where are the Baryons?

Our results show that the entire expected baryon content of dark matter halos can be detected or inferred using current observations. While the baryonic components (such as stellar mass or ICM gas) are more extended than the dark matter, they are still bound to their host halos, and there is no significant problem of baryons missing from halos. Therefore, the answer to the question, “Where are the baryons in dark matter halos?” is answered simply as: they are all found in the halos, distributed in various combinations between the central regions and the diffuse outskirts.

The size and frequency of virialized halos define the overall structure of matter in the universe. Because baryons populate in equal abundances galactic, group, and cluster halos, on large scales they represent excellent tracers of the overall dark matter distribution and structure. A relevant physical scale seems to be the halo virial radius: this scale separates the regimes where baryons do/do not trace the dark matter. On scales smaller than the virial radius, baryons are under-abundant, relative to their cosmic fraction, and this shortage is dependent on the overall mass of the halo. However, averaging on scales larger than  $r_{vir}$ , baryons match the dark matter distribution of the cosmos at a constant, unvarying fraction.

This suggests new ways to place constraints on the cosmology of the universe. Dark matter is notoriously difficult to detect or measure accurately, with the only direct method being with gravitational lensing. Baryons, however, emit or absorb radiation in a variety of measurable ways. The knowledge that baryons trace the underlying dark matter profile allows the use of baryon mass distributions to constrain the abundance and masses of halos (e.g., Ettori et al., 2009).

Furthermore, our results can help place constraints on the expected contents of baryon reservoirs exterior to halos. Examples of these interhalo components include the IGM, WHIM, and Ly $\alpha$  forest outside of galaxies and clusters, as well as the sparsely populated cosmic voids. If halos were deficient in baryons, then baryons in

these interhalo components would necessarily be overabundant, holding the additional baryons removed from halos. Because halos retain their relative baryon fractions, these diffuse components must also, and the baryonic mass in these components (as a whole) must match the total dark matter mass outside of halos in the cosmic fraction.

# Chapter 5

## Summary and Conclusions

In this thesis, we present a synthesis of observational constraints on the distribution and abundance of baryons in dark matter halos over a wide range of masses. Baryons, while only 16% of the total mass in the universe, are the most easily detectable form of matter and are incredibly important tools in understanding and observing the formation of structure and dark matter halos in the universe. Previous observations suggest halos are deficient in baryons relative to the cosmic fraction, a discrepancy known as the “Missing Baryon Problem”. We trace the baryon distribution in halos from galactic scales ( $M_{vir} = 10^{12} M_{\odot}$ ) to groups ( $M_{vir} = 10^{13} M_{\odot}$ ), and clusters ( $M_{vir} = 10^{14} - 10^{15} M_{\odot}$ ) to address the missing baryon problem and to obtain a global picture of the distribution of baryons relative to dark matter in the universe.

Our group and cluster gas mass data is comprised of a collection of X-ray and SZ measurements of the gas density, temperature, and pressure profiles in the ICM. The total mass is derived either through the assumption of hydrostatic equilibrium or by using weak lensing. When the gas fraction is not measured to the virial radius, we extrapolate the observed gas fraction using gas density profile slopes appropriate to the given halo mass or ICM temperature (Rasheed et al., 2011). Our galaxy cluster data comes from a compilation by Werk et al. (2014), and includes absorp-

tion measurements of the multiphase CGM, stellar masses, and ISM masses from HI surveys.

Our main results are as follows:

1. Although the gas fraction within  $r_{500}$  in clusters is significantly lower than the cosmic baryon fraction, the gas distribution is less centrally concentrated than dark matter, such that the gas fraction increases significantly when integrated to the cluster outskirts.
2. The gaseous ICM is more extended in low-mass halos, explaining why the gas fraction is observed to be particularly low within  $r_{500}$  in these halos. The gas fraction rises more steeply in groups and poor clusters than in massive clusters, and our extrapolations predict that the gas fraction of all groups and clusters should converge to the cosmic value near  $r_{vir}$ .
3. The cluster stellar fraction at any given radius is higher in groups and poor clusters, although in clusters of all sizes the fraction asymptotically approaches the “cosmic” stellar fraction  $0.01 \pm 0.004$  at high enough radius.
4. Observational constraints on the gas content of galactic halos find the cool CGM can account for 25 – 50% of the total baryonic mass. Current constraints of the stellar disk, ISM, and multiphase CGM are consistent with the galactic baryon fraction matching the cosmic value within the virial radius of  $L^*$  galaxies.
5. Combining the observed baryonic components of galaxy, group, and cluster halos, we show that dark matter halos contain the cosmic fraction of baryons within approximately the virial radius, across three orders of magnitude in halo mass.
6. The baryonic distribution of halos is not entirely self-similar. Baryons in less-massive halos are pushed farther into the outskirts of the shallow gravitational

well by feedback mechanisms, not reaching the cosmic fraction until higher radii. The abundance of different baryonic components (particularly stellar mass and gas) also changes with cluster mass.

7. The consistent baryon fraction in galactic and cluster halos suggests that cluster dark matter and baryonic masses could be composed entirely of matter originally in galactic halos which fell into cluster halos. Using the ratio of stellar fractions, we show that galactic halos contribute **no less than** 40% of the total matter of clusters.
8. The baryon distribution of the universe traces the dark matter distribution well, with no need for additional unseen or unbound reservoirs of baryons from halos. Averaged over scales larger than the virial radius, baryons map the total structure of the universe, and the baryonic mass of clusters is an effective proxy for the total mass.

Improvements on the precision of our results will come from better constraints of the ICM temperature profile at high radius (in clusters) and of the mass in the warm CGM phase (in galaxies). Additionally, further weak lensing calibrations are required to constrain the magnitude of the hydrostatic equilibrium bias on the total cluster mass.

The baryonic content of the universe, while energetically small, is what makes up all physical objects we observe; it drives astrophysical phenomena such as nucleosynthesis, chemistry, and planetary formation, and is what eventually gave rise to life. Yet, until recently, baryons have been overshadowed by dark matter as tools for studying cosmology of the low-redshift universe and the growth of large-scale structure. Our results show that the baryon distribution is an excellent proxy for the dark matter distribution, and represents a new way of approaching the growth and evolution of halos and structure in the universe.

# Bibliography

- Afshordi, N., Lin, Y.-T., Nagai, D., & Sanderson, A. J. R. 2007, *Monthly Notices of the Royal Astronomical Society*, 378, 293
- Anderson, M. E., Bregman, J. N., & Dai, X. 2013, *The Astrophysical Journal*, 762, 106
- Andersson, K., et al. 2011, *The Astrophysical Journal*, 738, 48
- Arnaud, M., Pointecouteau, E., & Pratt, G. W. 2007, *Astronomy and Astrophysics*, 474, L37
- Arnaud, M., Pratt, G. W., Piffaretti, R., Böhringer, H., Croston, J. H., & Pointecouteau, E. 2010, *Astronomy and Astrophysics*, 517, A92
- Bahcall, J. N., & Spitzer, L. J. 1969, *The Astrophysical Journal*, 156, L63
- Bahcall, N. A., & Kulier, A. 2014, *Monthly Notices of the Royal Astronomical Society*, 439, 2505
- Battaglia, N., Bond, J. R., Pfrommer, C., & Sievers, J. L. 2013, *The Astrophysical Journal*, 777, 123
- Behroozi, P. S., Conroy, C., & Wechsler, R. H. 2010, *The Astrophysical Journal*, 717, 379
- Bennett, C. L., et al. 2003, *The Astrophysical Journal Supplement Series*, 148, 1
- Bergeron, J. 1985, *Astronomy and Astrophysics*, 155, L8-L11 (1986)
- Bialek, J. J., Evrard, A. E., & Mohr, J. J. 2001, *The Astrophysical Journal*, 555, 597
- Bode, P., Ostriker, J. P., & Vikhlinin, A. 2009, *The Astrophysical Journal*, 700, 989
- Bonamente, M., Lieu, R., Mittaz, J. P. D., Kaastra, J. S., & Nevalainen, J. 2005, *The Astrophysical Journal*, 629, 192

- Booth, C. M., Schaye, J., Delgado, J. D., & Dalla Vecchia, C. 2012, *Monthly Notices of the Royal Astronomical Society*, 420, 1053
- Burns, J. O., Skillman, S. W., & O'Shea, B. W. 2010, *The Astrophysical Journal*, 721, 1105
- Cen, R., Miralda-Escude, J., Ostriker, J. P., & Rauch, M. 1994, *The Astrophysical Journal*, 437, L9
- Cen, R., & Ostriker, J. P. 1999, *The Astrophysical Journal*, 514, 1
- Chen, H.-W., Helsby, J. E., Gauthier, J.-R., Shectman, S. A., Thompson, I. B., & Tinker, J. L. 2010, *The Astrophysical Journal*, 714, 1521
- Dai, X., Bregman, J. N., Kochanek, C. S., & Rasia, E. 2010, *The Astrophysical Journal*, 719, 119
- Dave, R., Hernquist, L., Katz, N., & Weinberg, D. H. 1999, *The Astrophysical Journal*, 511, 521
- Dodelson, S. 2003, *Modern Cosmology* (San Diego: Academic Press)
- D'Odorico, S., & Savaglio, S. 1991, *Quasar Absorption Lines*, *Proceedings of the ESO Mini-Workshop held 20-21 February, 1991*. Organized by P.A. Shaver, E.J. Wampler and A.M. Wolfe., p.51
- Dunkley, J., et al. 2009, *The Astrophysical Journal Supplement Series*, 180, 306
- Durrer, R. 2008, *The Cosmic Microwave Background* (New York, NY: Cambridge University Press)
- Eckert, D., Ettori, S., Molendi, S., Vazza, F., & Paltani, S. 2013a, *Astronomy & Astrophysics*, 551, A23
- Eckert, D., Ettori, S., Molendi, S., Vazza, F., Roncarelli, M., Gastaldello, F., & Rossetti, M. 2013b, e-print arXiv:1310.8389
- Eckert, D., Molendi, S., Vazza, F., Ettori, S., & Paltani, S. 2013c, *Astronomy & Astrophysics*, 551, A22
- Eckert, D., et al. 2012, *Astronomy & Astrophysics*, 541, A57
- Eke, V. R., Cole, S., & Frenk, C. S. 1996, *M.N.R.A.S.*, 282, 263-280 (1996)
- Ettori, S., & Balestra, I. 2009, *Astronomy and Astrophysics*, 496, 343
- Ettori, S., Morandi, A., Tozzi, P., Balestra, I., Borgani, S., Rosati, P., Lovisari, L., & Terenziani, F. 2009, *Astronomy and Astrophysics*, 501, 61



- Giardini, S., et al. 2009, *The Astrophysical Journal*, 703, 982
- Grego, L., Carlstrom, J. E., Reese, E. D., Holder, G. P., Holzappel, W. L., Joy, M. K., Mohr, J. J., & Patel, S. 2001, *The Astrophysical Journal*, 552, 2
- Gruen, D., et al. 2013, eprint arXiv:1310.6744, 36
- Guo, Q., White, S., Li, C., & Boylan-Kolchin, M. 2010, *Monthly Notices of the Royal Astronomical Society*, 11
- Gupta, A., Mathur, S., Krongold, Y., Nicastro, F., & Galeazzi, M. 2012, *The Astrophysical Journal*, 756, L8
- High, F. W., et al. 2012, *The Astrophysical Journal*, 758, 68
- Hinshaw, G., et al. 2013, *The Astrophysical Journal Supplement Series*, 208, 19
- Hopkins, A. M., & Beacom, J. F. 2006, *The Astrophysical Journal*, 651, 142
- Ichikawa, K., et al. 2013, *The Astrophysical Journal*, 766, 90
- Iocco, F., Mangano, G., Miele, G., Pisanti, O., & Serpico, P. D. 2009, *Physics Reports*, 472, 1
- Israel, H., Reiprich, T. H., Erben, T., Massey, R. J., Sarazin, C. L., Schneider, P., & Vikhlinin, A. 2014, e-print arXiv:1402.3267, 2
- Kirkman, D., Tytler, D., Suzuki, N., OMeara, J. M., & Lubin, D. 2003, *The Astrophysical Journal Supplement Series*, 149, 1
- Komatsu, E., & Seljak, U. 2001, *Monthly Notices of the Royal Astronomical Society*, 327, 1353
- Lanzetta, K. M., Bowen, D. B., Tytler, D., & Webb, J. K. 1995, *The Astrophysical Journal*, 442, 538
- Lau, E. T., Kravtsov, A. V., & Nagai, D. 2009, *The Astrophysical Journal*, 705, 1129
- Linsky, J. L., Diplas, A., Wood, B. E., Brown, A., Ayres, T. R., & Savage, B. D. 1995, *The Astrophysical Journal*, 451, 335
- Linsky, J. L., et al. 1993, *The Astrophysical Journal*, 402, 694

- Mandelbaum, R., Seljak, U., & Hirata, C. M. 2008, *Journal of Cosmology and Astroparticle Physics*, 2008, 006
- Martin, A. M., Papastergis, E., Giovanelli, R., Haynes, M. P., Springob, C. M., & Stierwalt, S. 2010, *The Astrophysical Journal*, 723, 1359
- McCarthy, I. G., Bower, R. G., & Balogh, M. L. 2007, *Monthly Notices of the Royal Astronomical Society*, 377, 1457
- McGaugh, S. S., Schombert, J. M., de Blok, W. J. G., & Zagursky, M. J. 2010, *The Astrophysical Journal*, 708, L14
- Meléndez, J., & Ramírez, I. 2004, *The Astrophysical Journal*, 615, L33
- Meneghetti, M., Rasia, E., Merten, J., Bellagamba, F., Ettori, S., Mazzotta, P., Dolag, K., & Marri, S. 2010, *Astronomy and Astrophysics*, 514, A93
- Metzler, C. A., & Evrard, A. E. 1994, *The Astrophysical Journal*, 437, 564
- Moster, B. P., Somerville, R. S., Maubetsch, C., van den Bosch, F. C., Macciò, A. V., Naab, T., & Oser, L. 2010, *The Astrophysical Journal*, 710, 903
- Mukhanov, V. 2005, *Physical Foundations of Cosmology* (New York, NY: Cambridge University Press)
- Nagai, D., & Lau, E. T. 2011, *The Astrophysical Journal*, 731, L10
- Nagai, D., Vikhlinin, A., & Kravtsov, A. V. 2007, *The Astrophysical Journal*, 655, 98
- Navarro, J. F., Frenk, C. S., & White, S. D. M. 1996, *The Astrophysical Journal*, 462, 563
- Nelson, K., Rudd, D. H., Shaw, L., & Nagai, D. 2012, *The Astrophysical Journal*, 751, 121
- Niemann, H. B., et al. 1996, *Science*, 272, 846
- Oppenheimer, B. D., Davé, R., Katz, N., Kollmeier, J. A., & Weinberg, D. H. 2012, *Monthly Notices of the Royal Astronomical Society*, 420, 829
- Oppenheimer, B. D., Davé, R., Kereš, D., Fardal, M., Katz, N., Kollmeier, J. A., & Weinberg, D. H. 2010, *Monthly Notices of the Royal Astronomical Society*, 406, 2325

- Ostriker, J. P., Peebles, P. J. E., & Yahil, A. 1974, *The Astrophysical Journal*, 193, L1
- Peeples, M. S., Werk, J. K., Tumlinson, J., Oppenheimer, B. D., Prochaska, J. X., Katz, N., & Weinberg, D. H. 2014, *The Astrophysical Journal*, 786, 54
- Planck Collaboration. 2011, *Astronomy & Astrophysics*, 536, A11
- . 2013a, e-print arXiv:1303.5062
- . 2013b, eprint arXiv:1303.5076
- . 2013c, *Astronomy & Astrophysics*, 558, C2
- . 2013d, *Astronomy & Astrophysics*, 550, A131
- Prochaska, J. X., Weiner, B., Chen, H.-W., Mulchaey, J., & Cooksey, K. 2011, *The Astrophysical Journal*, 740, 91
- Rasheed, B., Bahcall, N., & Bode, P. 2011, *Proceedings of the National Academy of Sciences of the United States of America*, 108, 3487
- Ryden, B. 2003, *Introduction to Cosmology* (San Francisco: Addison Wesley)
- Sargent, W. L. W., Young, P. J., Boksenberg, A., & Tytler, D. 1980, *The Astrophysical Journal Supplement Series*, 42, 41
- Sheldon, E. S., et al. 2009a, *The Astrophysical Journal*, 703, 2217
- . 2009b, *The Astrophysical Journal*, 703, 2232
- Spergel, D., Flauger, R., & Hlozek, R. 2013, eprint arXiv:1312.3313
- Steidel, C. C., Erb, D. K., Shapley, A. E., Pettini, M., Reddy, N., Bogosavljević, M., Rudie, G. C., & Rakic, O. 2010, *The Astrophysical Journal*, 717, 289
- Steigman, G. 2006, *International Journal of Modern Physics E*, 15, 1
- Sun, M., Voit, G. M., Donahue, M., Jones, C., Forman, W., & Vikhlinin, A. 2009, *The Astrophysical Journal*, 693, 1142
- Sunyaev, R. A., & Zeldovich, Y. B. 1972, *Comments on Astrophysics and Space Physics*, Vol. 4, p.173

- Suzuki, T. K., Yoshii, Y., & Beers, T. C. 2000, *The Astrophysical Journal*, 540, 99
- Takizawa, M., & Mineshige, S. 1998, *The Astrophysical Journal*, 499, 82
- Thom, C., et al. 2012, *The Astrophysical Journal*, 758, L41
- Tumlinson, J., et al. 2011, *Science (New York, N.Y.)*, 334, 948
- Tytler, D., Fan, X. M., & Burles, S. 1996, *Nature*, 381, 207
- Umetsu, K., et al. 2009, *The Astrophysical Journal*, 694, 1643
- Vikhlinin, A., Kravtsov, A., Forman, W., Jones, C., Markevitch, M., Murray, S. S., & Van Speybroeck, L. 2006, *The Astrophysical Journal*, 640, 691
- von der Linden, A., et al. 2014, *ArXiv e-prints*
- Weinberg, S. 2008, *Cosmology* (New York, NY: Oxford University Press)
- Werk, J. K., Prochaska, J. X., Thom, C., Tumlinson, J., Tripp, T. M., O'Meara, J. M., & Peebles, M. S. 2013, *The Astrophysical Journal Supplement Series*, 204, 17
- Werk, J. K., et al. 2014, e-print arXiv:1403.0947, 19
- Zhu, G., & Ménard, B. 2013, *The Astrophysical Journal*, 773, 16